



Rock fines breakage by flow-induced stresses against drag: geo-energy applications

Sara Borazjani · Abolfazl Hashemi · Cuong Nguyen · Grace Loi · Thomas Russell · Nastaran Khazali · Yutong Yang · Bryant Dang-Le · Pavel Bedrikovetsky

Received: 7 October 2023 / Accepted: 23 April 2024
© The Author(s) 2024

Abstract The paper presents a strength-failure mechanism for colloidal detachment by breakage and permeability decline in reservoir rocks. The current theory for permeability decline due to colloidal detachment, including microscale mobilisation mechanisms, mathematical and laboratory modelling, and upscaling to natural reservoirs, is developed only for *detrital particles* with detachment that occurs against electrostatic attraction. We establish a theory for detachment of widely spread *authigenic particles* due to breakage of the particle-rock bonds, by integrating beam theory of particle deformation, failure criteria, and creeping flow. Explicit expressions for stress maxima in the beam yield a graphical technique to determine the failure regime. The core-scale model for fines detachment by breakage has a form of maximum retention concentration of the fines, expressing rock capacity to produce breakable fines. This closes the governing system for authigenic fines transport in rocks. Matching of the lab coreflood data by the analytical model for 1D flow exhibits two-population particle behaviour, attributed to simultaneous detachment and migration of authigenic and detrital fines. High agreement between the laboratory and modelling data for 16 corefloods validates the theory. The

work is concluded by geo-energy applications to (i) clay breakage in geological faults, (ii) typical reservoir conditions for kaolinite breakage, (iii) well productivity damage due to authigenic fines migration, and (iv) feasibility of fines breakage in various geo-energy extraction technologies.

Article Highlights

- Detachment of authigenic particles from rock surface by breakage during viscous flow.
- Critical velocity equation for all cases of particle detachment by tensile and shear-stress failure.
- Feasibility of clay detachment by breakage in 12 field cases of geo-energy engineering.

Keywords Bond breakage · Particle detachment · Failure criteria · Beam theory · Fines migration · Analytical model

Abbreviations

English letters

a	Semi-major axis of the spheroidal particle, L
b	Semi-minor axis of the spheroidal particle, L
C_c	Clay fraction
C_a	Total produced fines
c	Particle suspension concentration

S. Borazjani · A. Hashemi · C. Nguyen · G. Loi · T. Russell · N. Khazali · Y. Yang · B. Dang-Le · P. Bedrikovetsky (✉)
School of Chemical Engineering, The University of Adelaide, Adelaide, SA 5000, Australia
e-mail: pavel.bedrikovetski@adelaide.edu.au

c_{acc}	Accumulated outlet suspended particle concentration	X, Y, Z	Dimensionless Euclidean coordinates
E	Energy potential, $M L^{-1} T^{-2}$	x, y, z	Euclidean coordinates, L
F_d	Drag force, $M L T^{-2}$	Greek letters	Drift delay factor
F_e	Maximum electrostatic force, $M L T^{-2}$	α	Aspect ratio of the particle
f_d	Shape factor for drag	α_s	Formation damage coefficient
f_M	Shape factor for moment	β	Fluid salinity, $molL^{-3}$
g	Breakage regime function	γ	Detached concentration between two consecutive velocities U_{n-1} to U_n
h	Particle-surface separation distance, L	$\Delta\sigma_n$	Bond ratio
I	Moment of inertia, L^4	δ	Strength number
J	Impedance	η	Strength-drag number
k_0	Initial absolute permeability, L^2	κ	Filtration coefficient, L^{-1}
L	System length, L	λ	Filtration coefficient, L^{-1}
l_n	Lever arm for electrostatic force, L	μ_f	Fluid viscosity, $M L^{-1} T^{-1}$
M_b	Bending moment, $M L^2 T^{-2}$	ν_c	Coulomb friction coefficient
PV	Pore volume injected	ξ	Dimensionless parameter proportional to χ and depending on ν
p	Pressure, $M L^{-1} T^{-2}$	Σ	Tensile stress, $M L^{-1} T^{-2}$
R^2	Coefficient of determination	σ_0	Detachable fines concentration
r_b	Beam radius (or bond radius), L	$\sigma_{1,2,3}$	Principal stresses, $M L^{-1} T^{-2}$
r_s	Effective particle radius, L	σ_{cr}	Critical retention function
r_w	Well radius, L	σ_s	MRF
S^0	Normalized shear stress at the middle of the beam, $M L^{-1} T^{-2}$	σ_x	Strained particle concentration
S^1	Normalized shear stress at the boundary of the beam, $M L^{-1} T^{-2}$	σ_y	Normal stress in x-direction, $M L^{-1} T^{-2}$
S_0	Shear strength, $M L^{-1} T^{-2}$	σ_z	Normal stress in y-direction, $M L^{-1} T^{-2}$
T	Temperature, Θ	T	Normal stress in z-direction, $M L^{-1} T^{-2}$
t	Time, T	τ_{xy}	Shear stress, $M L^{-1} T^{-2}$
T^0	Normalized tensile stress at the middle of the beam, $M L^{-1} T^{-2}$	τ_{xz}	Shear stress at y-plane towards x-direction, $M L^{-1} T^{-2}$
T^1	Normalized tensile stress at the boundary of the beam, $M L^{-1} T^{-2}$	τ_{yz}	Shear stress at z-plane towards x-direction, $M L^{-1} T^{-2}$
T_0	Tensile strength, $M L^{-1} T^{-2}$	ν	Shear stress at z-plane towards y-direction, $M L^{-1} T^{-2}$
U	Darcy's velocity, MT^{-1}	ϕ	Poisson's ratio
U^b	Breakage Darcy's velocity, MT^{-1}	χ	Porosity
V	Interstitial fluid velocity, MT^{-1}	Subscript c	Shape-Poisson number
			Cylinder

cr	Critical
k	Index that corresponds to the two populations
m	Maximum
n	Index that is attributed to the injection velocity steps
St	Stabilised
Superscript b	Breakage
e	Electrostatic or detrital particles
Abbreviations	CBM Coal bed methane
CFD	Computational fluid dynamics
DLVO	Derjaguin, Landau, Verwey, Overbeek
GWP	Geothermal water production
HF	Hydraulic fracturing
HFw	Hydraulic fracturing using water
MRF	Maximum retention function
NG	Natural gas production
PDF	Probability distribution function
WI	Water injection into aquifers
WP	Water production from aquifers

1 Introduction

The geomechanics of rock failure under high stress with consequent permeability alteration is a wide and long-studied topic in geo-energy engineering. An incomplete list includes mining operation studies in gas-bearing coals (Wang et al. 2022a; Xu et al. 2022), geo-engineering applications in granites (Kumari et al. 2019), loading of lamellar continental shales (Duan et al. 2022), cyclic hydraulic fracturing for geothermal reservoir stimulation (Li et al. 2022), drainage technology of CBM fields (Xue et al. 2022), mechanical failure of hydrate-bearing sediments (Hou et al. 2022), and wellbore stability during drilling (Wang et al. 2022b). Yet, the studies of detachment of a single reservoir fines by breakage and the migration-induced permeability decline are not available.

However, transport in porous and fractured media strongly depend on colloidal detachment, migration, straining, and consequent permeability decline (Chen

et al. 2008; Teitelbaum et al. 2022; Cao et al. 2023). The permeability decrease yields well productivity and injectivity decline, while preferential permeability decline in high-conductivity layers and patterns of natural reservoirs uniformises the flux and increases sweep efficiency (Bedrikovetsky 2013). Mineral dissolution and precipitation reactions during injection of CO₂ or hydrogen into underground gas storages, cause fines mobilisation and migration; the resulting sweep enhancement leads to the storage capacity increase (Iglauer et al. 2015, 2021, 2022; Alzate-Espinosa et al. 2023). Detachment of colloidal and nano particles highly affects oil and gas production under migration of natural reservoir fines, water injection into aquifers and petroleum reservoirs, geothermal energy recovery, coal bed methane production, storage of fresh and hot water in aquifers, propagation of contaminants, bacteria and viruses, invasion of ocean into aquifers, soil erosion and construction collapse, and analysis of seismic earthquake events (Zhao et al. 2014; Fox et al. 2018; Drummond et al. 2019; Hu et al. 2021; Lehman et al. 2021; Liao et al. 2021; Lu et al. 2021; Sun and Xiang 2021; Wurgaft et al. 2021).

Typical migrating fines comprise clays, while silt, silica, and coal particles can be mobilised too (Fox et al. 2018; Farrell et al. 2021; Cao et al. 2023). Two types of natural fines are distinguished in the rocks: *authigenic fines*, that have been grown up on the grain surfaces during geological times and are bonded to the surface, and the *detrital fines* that have been carried by subterranean waters to a given reservoir point and attached to the rock surface (Wilson and Pittman 1977; Appelo and Postma 2004; Farrell et al. 2021). Detrital kaolinite is attached to the grain surface by electrostatic attraction (Fig. 1a), while the authigenic kaolinite bond the grain surface (Fig. 1b). The detachment of detrital particles against electrostatic attraction and authigenic particles by breakage, under high velocities in pore throat is presented in Fig. 1c.

Figures 2 and 3 present evidence of the fines breakage off the grain surfaces due to viscous flow. Figure 2 shows a number of pores before and after the flow; breakage of the matrix with liberation of some fines is indicated by the arrow 3.

Figure 3 presents SEM image of fines collected from the effluent during CO₂ flood. The image shows a kaolinite fine, likely detached by breakage of the carbonate-cement particle-grain bond, and the quartz particle detached against the electrostatic attraction.

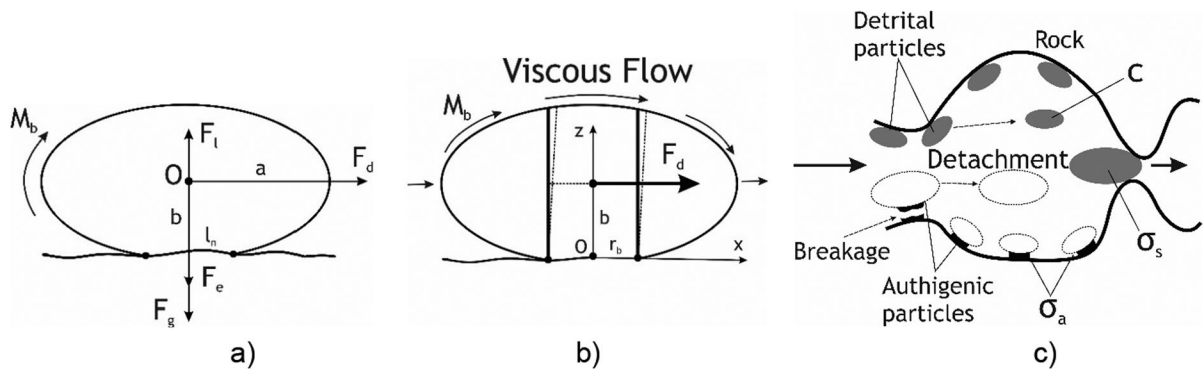


Fig. 1 Detachment for detrital and authigenic clay particles: **a** force (torque) balance at attached detrital fine; **b** representation of attached authigenic particle by deformable beam (Obermayr

et al. 2013); **c** schematic for detachment against electrostatic attraction and by breakage at the pore scale

Fig. 2 Evidence of fines detachment from the rock by breakage: **a** prior to viscous flow; **b** after the flow. In **a** and **b**, arrow 3 delineates breakage of a grain's structure (Wang et al. 2022d)

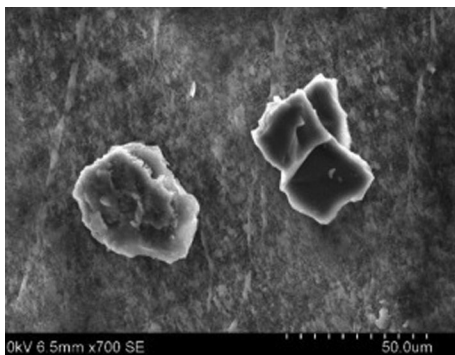
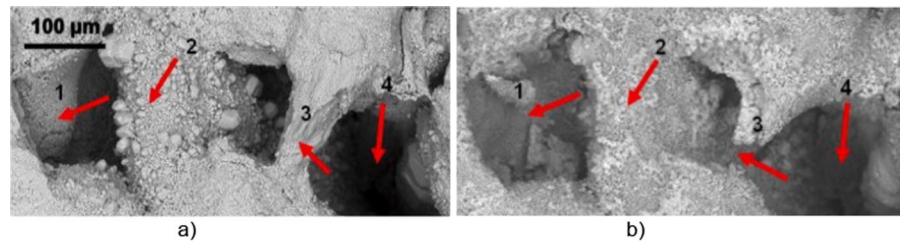


Fig. 3 SEM images a quartz fine (right) and kaolinite fine with carbonate cement (left) produced from Berea core sample during 60 g/L NaCl water-saturated super critical CO_2 injection (Othman et al. 2019)

Current mathematical and lab modelling for *detachment of detrital fines* is based on the mechanical equilibrium of a particle situated on the solid substrate; Fig. 1a shows drag, electrostatic, lift, and gravity forces exerting on an isolated particle. Presence of a second phase adds capillary force, which is wettability dependent (Roshan et al. 2016; Siddiqui et al.

2019). The linear-kinetics model for fines detachment assumes that detachment rate is proportional to the difference between current and equilibrium retention concentrations, with an empirical proportionality coefficient that is equal to the inverse of detachment time (Bradford et al. 2013; Johnson and Pazmino 2023). In the alternative theory, the maximum retention concentration of the attached fines, as a function of velocity, salinity, temperature, and pH, defines fines detachment (Bedrikovetsky et al. 2011, 2012). This maximum retention function (MRF) closes the system of governing equations for colloidal transport in porous media and yields several exact solutions for 1D flows (Polyanin 2002; Polyanin and Zaitsev 2012). The MRF model has been validated by extensive laboratory studies and is widely used for prediction of colloidal transport (Yuan and Shapiro 2011; Guo et al. 2016; Yuan and Moghanloo 2018, 2019; Zhai and Atefi-Monfared 2021).

Detachment of authigenic fines by breakage under flows in porous media has been observed by Turner and Steel (2016) and Wang et al. (2020) during well acidizing, by Tang et al. (2016) and Othman et al. (2018) for cement dissolution in sandstones, by Hadi

et al. (2019) for carbonate rock dissolution in water, by Mishra and Ojha (2016) during sand production, and by Liu et al. (2019) for hydraulic fracturing. Yet, a geo-mechanical analysis and mathematical model for authigenic particle detachment and migration is not available.

The current paper fills the gap. A novel micro-scale model for authigenic particle detachment is derived by integration of beam theory of elastic particle deformation and strength failure with viscous flow model around the attached fines. Introduction of tensile-stress and tensile-shear diagrams allows determining the regime of particle-rock-bond failure. The breakage condition has a form of breakage velocity versus micro-scale geo-mechanical parameters, which yields maximum concentration of authigenic particles versus velocity, that closes the system of governing equations. We successfully match 16 coreflood tests under piecewise-constant increasing rate by the analytical model for colloidal flow with breakage; the data are taken from the literature. The laboratory-based analytical model for particle detachment by breakage (i) shows feasibility of authigenic fines mobilisation in geological faults, (ii) allows calculating the fraction of detachable authigenic fines in natural rocks and estimation the range of breaking velocities, (iii) permits predicting of well productivity decline, and (iv) claims that fines breakage is feasible in major geo-energy technologies.

Figure 4 illustrates the structure of the paper. Section 2 derives the microscale mechanical conditions of attached fines mobilisation by breakage. Section 3 defines maximum retention concentration (MRF) for authigenic fines as a rock-scale model for fines mobilisation by breakage and the analytical model for 1D flows. Section 4 matches the laboratory coreflood data by the analytical model and validates the breakage-detachment model. Section 5 investigates breakage of authigenic clays in geological faults. Section 6 determines the fractions of detachable fines and of authigenic particles using the analytical model. Section 7 recalculates lab results into the well-productivity data. Section 8 investigates the feasibility of fines breakage in various technological geo-energy processes. Section 9 discusses the limitations of the developed breakage-detachment model. Section 10 concludes the paper.

2 Model for beam deformation under creeping flow

Derivation of the microscale model for fines detachment by breakage during viscous flow encompasses mechanical equilibrium of attached particle (Sect. 2.1 and Appendix 1), expressions for stress maxima (Sect. 2.2 and Appendix 2), and graphical classification of the breakage regimes (Sect. 2.3).

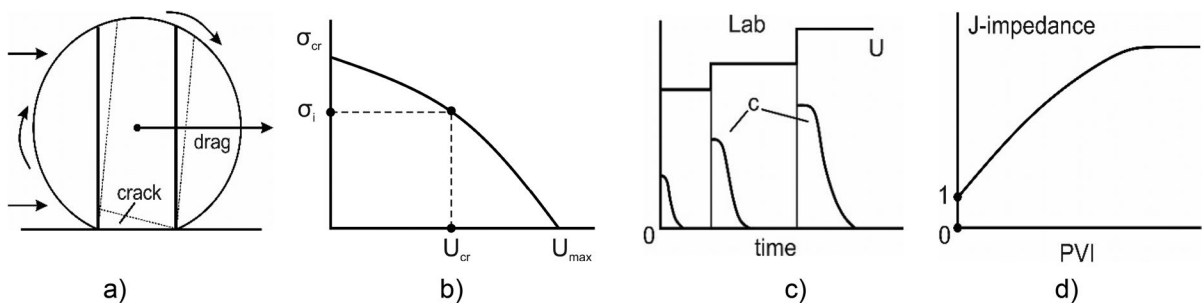


Fig. 4 The logic diagram of this work: **a** breakage criteria based on elastic beam theory; **b** maximum retention concentration of attached particles based on the breakage criteria; **c**

matching the lab data by the analytical model, which is based on maximum retention function; **d** lab-based well impedance prediction

2.1 Definition of mechanical equilibria of detaching particles

The model assumes single-phase flow of Newtonian fluid around an elastic particle of spheroidal form with circular contact area between the particle and the rock, negligible effect of particle deformation on the drag and its moment, and negligible stresses in the particle outside its stem (beam) part. The lift and gravitational forces are negligible if compared with the drag. Particles exhibit brittle behaviour with breakage. The failure criterium is the point where the tensile (shear) exceeds the strength the tensile (shear) stress.

The microscale model of a single fine detachment by breakage, presented in this section, integrates beam theory for elastic cylinder deformation (Timoshenko and Goodier 1970) with strength failure criteria for particle-rock bond (Fjaer et al. 2008; Jaeger et al. 2009) and creeping flow around the particle (Tu et al. 2018). The model assumes negligible lift exerting the particle from the flux and low beam deformations under slow Darcy's flows in porous media. We discuss spheroidal and thin-cylinder shapes for kaolinite, chlorite, and silica fines, and long cylinders for illite fines (Appelo and Postma 2004). A circular particle-rock contact area is assumed. The rock deformation outside the beam stem is significantly lower than beam deformation; this supports the assumption that maximum stress in the contact particle-substrate area due to drag is fully determined by the deformation of the cylindrical beam with the base on substrate (Obermayr et al. 2013; Wagner et al. 2016; Chen et al. 2022) (Fig. 1b). Following the lab data by Abou-sleiman et al. (2016), Han et al. (2019), Yang et al.

(2019), Feng et al. (2020), Ren et al. (2021), brittle breakage of the particle-substrate bond is assumed.

Drag F_d and its moment M_b for oblate spheroidal and cylindrical particles are extensions of the Stokes formula that is valid for spheres (Ting et al. 2021, 2022). The dimensionless shape factors are calculated from numerical solution of Navier-Stokes flow around the particle:

$$\begin{aligned} F_d &= 6\pi\mu_f r_s V f_d(\alpha_s), \\ M_b &= F_d b f_M(\alpha_s) = 6\pi\mu_f r_s V f_d(\alpha_s) b f_M(\alpha_s), \\ \alpha_s &= b/a \end{aligned} \quad (1)$$

where a and b are the semi-major and semi-minor of spheroid, respectively, α_s is the aspect ratio, μ_f is the fluid viscosity, r_s is the particle radius, and V is the interstitial flow velocity. We derive the empirical formulae for drag and torque factors— $f_d(\alpha_s)$ and $f_M(\alpha_s)$ —for long cylinders, given by Eqs. (20) and (21), based on numerous runs of CFD software ANSYS/CFX.

The drag and torque (1) determine an external load in Timoshenko's solution for elastic beam, given by Eqs. (22–25). More detailed formulation of 3D elasticity problem is available from Hashemi et al. 2023a. The principal stresses σ_1 , σ_2 , and σ_3 are calculated as eigen values of the stress tensor (26); their maxima are determined using the Mohr circles and are determined by Eq. (27). Finally, maximum tensile (σ) and shear (τ) stresses are:

$$\max \sigma = \sigma_3, \quad \max \tau = \frac{\sigma_1 - \sigma_3}{2} \quad (2)$$

The expressions for tensile and shear stresses over the beam base follow from the solution of elastic beam deformation (22–25); here axi are shown in Fig. 1b:

$$\frac{\sigma_3}{T_0} = \frac{1}{\kappa} \left(X - \sqrt{X^2 + \chi \left(1 - X^2 - \frac{(1-2\nu)}{(3+2\nu)} Y^2 \right)^2} + \chi \frac{4(1+2\nu)^2}{(3+2\nu)^2} (XY)^2} \right) \quad (3)$$

$$\frac{\sigma_1 - \sigma_3}{2S_0} = \frac{\eta}{\kappa} \sqrt{X^2 + \chi \left(1 - X^2 - \frac{(1-2\nu)}{(3+2\nu)} Y^2 \right)^2} + \chi \frac{4(1+2\nu)^2}{(3+2\nu)^2} (XY)^2 \quad (4)$$

where X and Y are dimensionless coordinates, T_0 and S_0 are the tensile and shear strengths, respectively, and ν is the Poisson ratio. Here the dimensionless groups κ , χ , and η reflecting the interaction between the creeping flow around an attached particle and elastic deformation inside the particle—*strength-drag number* κ , *shape-Poisson number* χ , and *strength number* η —are defined as

$$\frac{1}{\kappa} = \frac{F_d}{2T_0} \frac{r_b b f_M}{I} = \frac{F_d}{2T_0} \frac{\delta \alpha_s f_M}{I},$$

$$\chi = \left[\frac{r_b}{b f_M} \frac{3 + 2\nu}{4(1 + \nu)} \right]^2, \quad \eta = \frac{T_0}{S_0}, \quad \delta = \frac{r_b}{a}, \quad (5)$$

$$X = \frac{x}{r_b}, \quad Y = \frac{y}{r_b}$$

where r_b is the bond radius, I is the moment of inertia, and x and y are dimensional coordinates.

The *strength-drag number* κ is proportional to the ratio between the tensile strength T_0 and the average pressure imposed by drag and incorporates the bond δ and aspect α_s ratios. The *shape-Poisson number* χ includes the bond δ and aspect α_s ratios along with the Poisson's ratio ν .

Breakage of particle-rock bond is defined by the strength failure criterium, where either tensile or shear stress reaches the corresponding strength value; this maximum normalised stress becomes equal to one, while another normalised stress remains less than one upon the breakage (Jaeger et al. 2009):

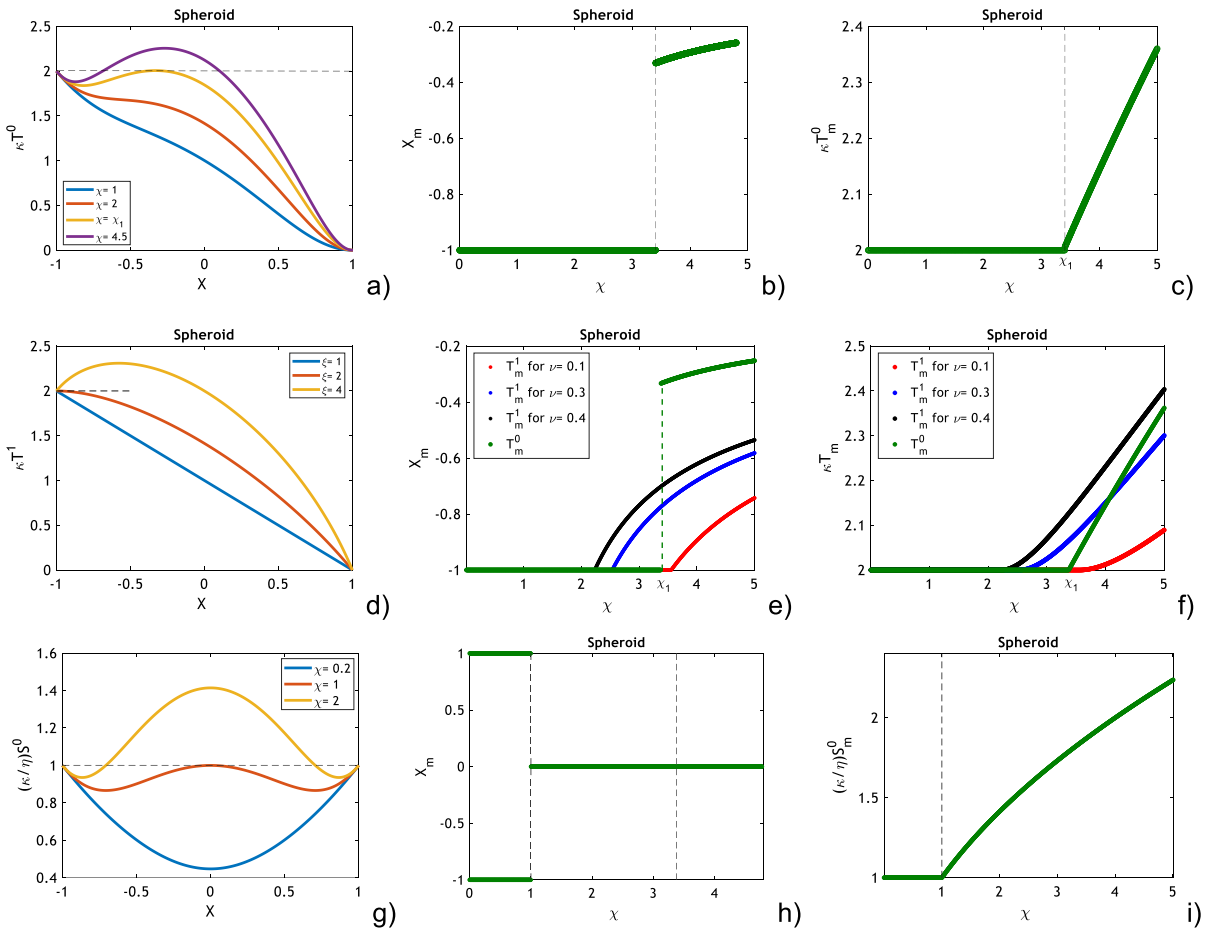


Fig. 5 Maximum dimensionless stresses at the beam base versus shape-Poisson number χ : **a** maximum tensile stress along the axes $Y=0$; **b** maximum tensile stress at the beam bound-

ary; **c** maximum shear stress along the axes $Y=0$; **d** Maximum shear stress along the beam boundary

$$\max_{x^2+y^2 \leq 1} \frac{-\sigma_3(X, Y)}{T_0} \leq 1, \quad \max_{x^2+y^2 \leq 1} \frac{\sigma_1(X, Y) - \sigma_3(X, Y)}{2S_0} \leq 1 \tag{6}$$

2.2 Derivation of stress maxima

Consider maxima of both tensile and shear stresses, which are given by Eqs. (3, 4). The detailed derivations are presented in Hashemi et al. (2023a). If maxima points (X_m, Y_m) are located inside the base circle, $X_m^2 + Y_m^2 < 1$, partial derivatives of both expressions (3, 4) over Y must be zero. It is possible to show that only along the middle of the beam base $Y=0$, partial derivatives over Y are equal zero and second partial derivatives over Y are negative. Therefore, all maxima inside the base circle $X_m^2 + Y_m^2 < 1$ are reached along the middle of the base, i.e., axis $Y=0$. Otherwise, tensile or shear stresses reaches maxima at the beam base over the boundary $X_m^2 + Y_m^2 = 1$.

The stresses along the beam middle and its boundary are functions of variable X alone. The profiles for tensile stress in the middle of the beam, tensile stress at the beam boundary, and shear stress at the boundary are shown in Fig. 5a, d, and g, respectively. Figure 5b, e, and h show the point X_m where maximum is reached, for those 3 cases. Figure 5c, f, and i present the maxima values.

Tensile stress $T^0(X, \chi)$ reaches maximum in the advanced point $X_m = -1$ and then monotonically decreases for small shape-Poisson numbers. At the bifurcation value $\chi_1 = 3.38$ the profile reaches second maximum at $X_{m1} = -0.33$. For $\chi > \chi_1$, maximum point moves to the right, and maximum increases. Maximum point X_m and corresponding tensile stress maximum T_m^0 depend on shape-Poisson number alone. The maximum point and its value are calculated from the conditions of zero first derivative and negative second derivative in X :

$$T_m^0(\chi) = \frac{1}{\kappa} \begin{cases} 2, & \chi \leq \chi_1 \\ -X_m(\chi) + \sqrt{X_m^2 + \chi(1 - X_m^2)^2}, & \chi > \chi_1 \end{cases}; \quad X_m = \begin{cases} -1, & \chi \leq \chi_1 \\ -\sqrt{-\frac{\sqrt{(4\chi-1)(4\chi-9)}-4\chi+3}{8\chi}}, & \chi > \chi_1 \end{cases} \tag{7}$$

Profile of tensile stress over the beam boundary also depends on parameter ξ alone that incorporates χ and v :

$$T_m^1(\chi, v) = \frac{1}{\kappa} \begin{cases} 2, & \xi \leq 2 \\ \xi(\xi - 1)^{-0.5}, & \xi > 2 \end{cases}; \quad X_m = \begin{cases} -1, & \xi \leq 2 \\ -(\xi - 1)^{-0.5}, & \xi > 2 \end{cases}; \tag{8}$$

$$\xi = \chi \frac{4(1 + 2v)^2}{(3 + 2v)^2}$$

The profile for $T^1(X, \xi)$ reaches maximum at advanced point $X_m = -1$ and monotonically decreases for $X > -1$ from advanced point $X_m = -1$ for small ξ . From bifurcation value $\xi = 2$ on, $T^1(X, \xi)$ loses monotonicity, maximum point X_m moves from advanced point $X_m = -1$ to the right.

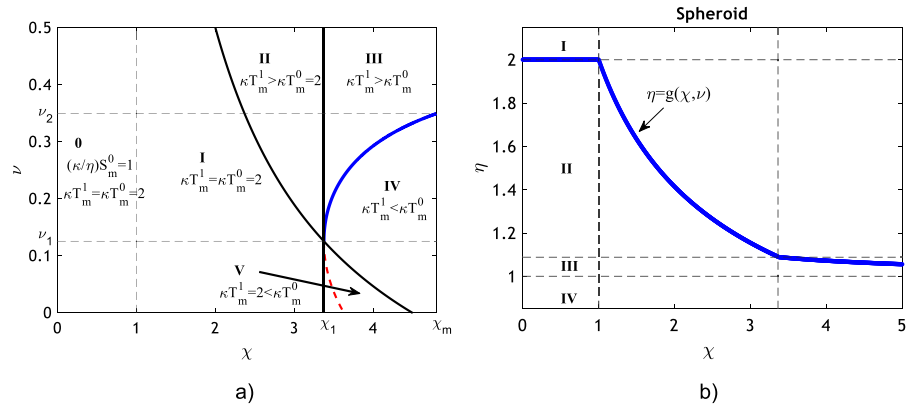
At low χ , maximum for shear in the base middle is reached at advanced and receded points. This occurs until bifurcation value $\chi = 1$, where X_m jumps into the origin $X_m = 0$. For $\chi > 1$, the maximum point for shear stress in the base middle remains in origin and monotonically increases:

$$S_m^0(\chi) = \frac{\eta}{\kappa} \begin{cases} 1, & \chi < 1 \\ \sqrt{\chi}, & \chi > 1 \end{cases}; \quad X_m = \begin{cases} \pm 1, & \chi < 1 \\ 0, & \chi > 1 \end{cases}; \quad \eta = \frac{T_0}{S_0} \tag{9}$$

Maximum of shear over the boundary is lower than the shear maximum in the base middle for all values of shape-Poisson numbers and Poisson’s ratio— $S_m^1(\chi, v) < S_m^0(\chi, v)$ —and is not considered to fulfil failure criteria.

Equations (7–9) show that stress maxima along the axis $Y=0$ are determined by aspect-Poisson number χ alone, while the maxima at the beam boundary

Fig. 6 Classification of bond breakage regimes by tensile and shear stresses: **a** tensile stress diagram; **b** shear-tensile diagram



are determined by both aspect-Poisson number χ and Poisson’s ratio ν .

2.3 Classification of breakage regimes

Depending on shape-Poisson number and Poisson’s ratio, either of three stresses (7), (8), or (9) can exceed the other two and fulfil the strength failure criteria (6). Let us first define the largest from the two tensile stress maxima, (7) or (8). Their equality $T_m^0(\chi, \nu) = T_m^1(\chi, \nu)$ divides plane (χ, ν) , which further in the text we call tensile stress diagram, into 5 regions. Black curve corresponds to $\xi = 2$. Blue and red curves are calculated from Eqs. (7) and (8) for $\xi > 2$:

$$\nu_m(\chi) = \frac{3\sqrt{(\kappa T_m^0(\chi))^2 \pm \kappa T_m^0(\chi)\sqrt{(\kappa T_m^0(\chi))^2 - 4} - \sqrt{8\chi}}}{4\sqrt{2\chi} - 2\sqrt{(\kappa T_m^0(\chi))^2 \pm \kappa T_m^0(\chi)\sqrt{(\kappa T_m^0(\chi))^2 - 4}}} \tag{10}$$

and correspond to positive and negative values of the root in Eq. (10). Along the red curve, inequality $\xi > 2$ holds, while domain V is located below black curve, so the red curve must be ignored.

The black curve, the vertical straight line $\chi = \chi_1$, and the blue curve divide (χ, ν) plane into 5 domains, depending on superiority of either of the two tensile stress maxima (Fig. 6a). The three lines cross in one point $(\chi = \chi_1, \nu = \nu_1)$ where $\nu_1 = 0.125$ is obtained from Eq. (10).

Now let us determine whether shear S_m^0 exceeds maximum of two tensile stresses. Define the breakage regime function

$$g(\chi, \nu) = \frac{T_m(\chi, \nu)}{S_m^0(\chi)} > \frac{T_0}{S_0} = \eta; \tag{11}$$

$$T_m(\chi, \nu) = \max \{ T_m^0(\chi, \nu), T_m^1(\chi, \nu) \}$$

At breakage, maximum normalised stress is equal one. Therefore, as it follows from Eq. (6), the breakage occurs due to tensile stress if $g(\chi, \nu) > \eta$. Otherwise, the breakage occurs due to shear stress. Further in the text, (χ, η) -plane with the curve $\eta = g(\chi, \nu)$ is called the shear-tensile diagram (Fig. 6b).

For all χ and ν values, breakage regime function exceeds one and does not exceed two. Depending on stress η and shape-Poisson numbers, and Poisson’s ratio, the breakage curve exhibits 4 cases presented in plane (χ, η) :

- I. For strength ratios exceeding 2, particles are detached by shear stress for all values of χ and ν ;
- II. For strength ratios below two and above one, the particles are detached by shear stress for shape-Poisson number χ that does not exceed the value determined by $g(\chi, \nu) = \eta$;
- III. For strength ratios below two and above one, the particles are detached by tensile stress for shape-Poisson number χ that exceeds the value determined by $g(\chi, \nu) = \eta$;

IV. For strength ratios lower than one, particles are detached by tensile stress for all values of χ and v .

So, either of the 5 domains in tensile-stress diagram determines maximum tensile stress, and then either of the 4 cases in tensile-shear diagram determines which stress causes the breakage. For either of three stress cases (7), (8), or (9), the normalised stress is equal one, allowing calculating stress-drag number κ . For the cases of domination of normalised tensile stress in the middle, tensile stress on the boundary, and shear stress in the middle, the formulae for strength-drag numbers κ are:

$$\kappa = \begin{cases} 2, & \chi \leq \chi_1 \\ \sqrt{-\frac{\sqrt{(4\chi-1)(4\chi-9)}-4\chi+3}{8\chi}} + \sqrt{\left(\sqrt{-\frac{\sqrt{(4\chi-1)(4\chi-9)}-4\chi+3}{8\chi}}\right)^2 + \chi\left(1 - \left(\sqrt{-\frac{\sqrt{(4\chi-1)(4\chi-9)}-4\chi+3}{8\chi}}\right)^2\right)^2} & \chi > \chi_1 \end{cases} \quad (12)$$

$$\kappa = \begin{cases} 2, & \xi \leq 2 \\ \xi(\xi - 1)^{-0.5}, & \xi > 2 \end{cases}; \quad \xi = \chi \frac{4(1 + 2v)^2}{(3 + 2v)^2} \quad (13)$$

$$\kappa = \frac{T_0}{S_0} \begin{cases} 1, & \chi < 1 \\ \sqrt{\chi}, & \chi > 1 \end{cases}, \quad (14)$$

3 Macroscale model for fines migration with detachment by breakage

This section defines rock-scale model for detachment of authigenic fines by breakage (Sect. 3.1) and its implementation into transport equations for the authigenic particles (Sect. 3.2).

3.1 Maximum retention function as a rock-scale detachment model

Substitution of drag from Eq. (1) into the expression for strength-drag number (5) allows for exact expression for the breakage velocity:

$$U_{cr}^b = \frac{\delta\phi T_0 r_b^2}{12\alpha_s f_M f_d \mu_f r_s} \kappa^{-1} \quad (15)$$

where κ is given by either of Eqs. (12–14). Consider the manifold of the particles attached to rock surface. The particles are stochastically distributed by fluid velocity around them near to asperous rock surface in pores of different forms and sizes, aspect, Poisson’s,

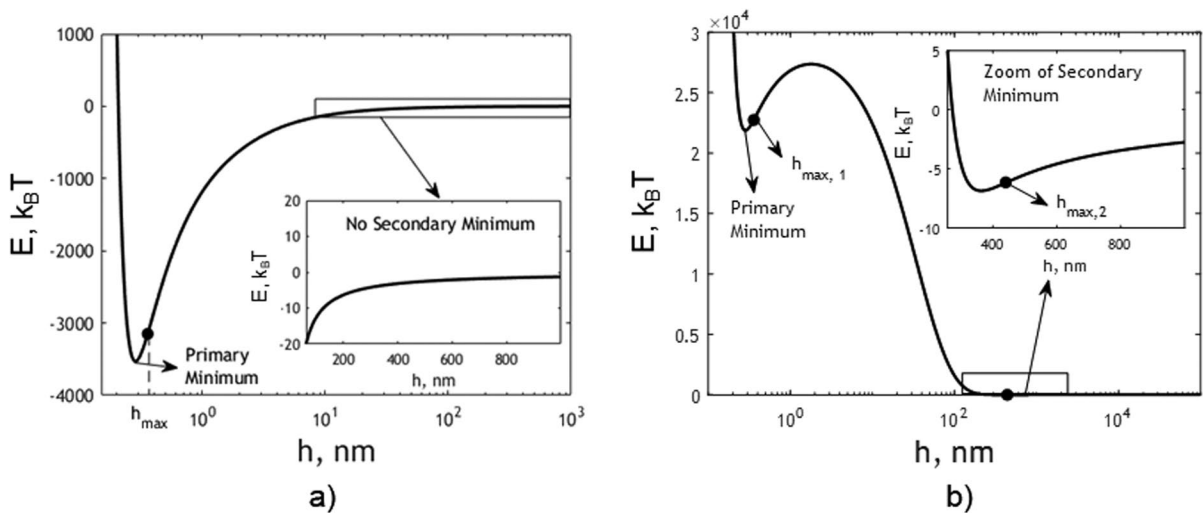


Fig. 7 DLVO energy profiles: **a** coal fines and coal substrate; **b** kaolinite fines and silica substrate

and bond ratios, sizes, strength, and bond radii. However, Eq. (15) determines the critical breakage velocity for each particle, defining whether the particle remains attached or breaks off the rock at a given flow velocity U . The concentration of the particles attached to rock at a given velocity is called the breakage maximum retention function (MRF) $\sigma_{cr}^b(U)$. MRF can be obtained by upscaling of Eq. (15) accounting for probabilistic distributions of coefficients δ , r_b , α_s , and r_s .

The maximum retention function for detachment against electrostatic DLVO attraction for detrital particles is determined by the torque balance between drag and electrostatic DLVO forces (Bradford et al. 2013):

$$\begin{aligned} M_b &= 6\pi\mu_f r_s V f_d(\alpha_s) b f_M(\alpha_s) = F_e(h) l_n, \\ F_d &= 6\pi\mu_f r_s V f_d(\alpha_s) = \nu_c F_e(h), \end{aligned} \tag{16}$$

where h is the distance between the particle and substrate and ν_c is the Coulomb friction coefficient.

Figure 7 presents the energy profile for the DLVO forces (Israelachvili 2015). Figure 7a shows the potential for coal fines and substrate with one energy minimum, while Fig. 7b shows two minima of the energy profile. During favourable attachment, the particle moves to the left from zero energy state to a single primary minimum. During unfavourable attachment, the particle moves to the left from zero energy to shallow secondary energy minimum and needs to overcome the energy barrier to get into primary energy minimum (Fig. 7b).

Assuming that authigenic and detrital fines detach independently, the overall MRF is the total of individual ones:

$$\sigma_{cr}(U) = \sigma_{cr}^e(U) + \sigma_{cr}^b(U), \quad \Delta\sigma(U_n) = \sigma_{cr}(U_{n-1}) - \sigma_{cr}(U_n) \tag{17}$$

The total MRF defines the mobilised concentration by velocity increase from U_{n-1} to U_n . After mobilisation, the detached fines migration is described by system of population balance accounting for particle capture by the rock. MRF defines initial concentration of detached particles after abrupt change of flow rate.

3.2 Macroscale analytical model for colloidal transport in porous media

1D problems for fines migration with any arbitrary particle capture (filtration) function $\lambda(\sigma_s)$ and suspension function $f(c)$ allow for exact solutions (Polyanin and Manzhirov 2006; Polyanin and Zaitsev 2012). In the case of continuous rate increase, MRF determines the sources term in mass balance, closing the governing system for colloidal-suspension transport (fines migration) in porous media (Bedrikovetsky et al. 2019). Here, for the sake of simplicity, we discuss the model with constant filtration coefficient $\lambda = \text{const}$ and $f(c) = c$, in order to treat the limited literature information on the corefloods with piecewise-constant increasing velocity.

Appendix 3 presents system of governing equations, which consists of the mass balance of suspended and strained particles (30), straining rate (31), and Darcy’s law accounting for permeability decline due to particle straining (32). For the case the corefloods with piecewise-constant increasing velocity $U_0=0, U_1, U_2, \dots$, fines detachment occurs at moments of switching from velocity U_{n-1} to $U_n, n=1, 2, 3, \dots$, which is expressed by initial condition (33). The exact solution for 1D flow problem is expressed by Eqs. (35) and (36). The exact solution allows for explicit expression of impedance (38). Next section uses Eqs. (35) and (38) to treat the lab data on breakthrough concentration $c(1,t)$ and dimensionless pressure drop (impedance) $J(t)$ measured during the multi-rate corefloods.

4 Laboratory study and model validation

Huang et al. (2017) used core sample from a coal seam reservoir located in the southern part of the Qinshui Basin (China) for coreflooding. The laboratory study was comprised of water injection with 2% (weight percent) of KCl into the anthracite coal core with permeability 21 mD and porosity 0.08. Core length was 5.16 cm. Figure 8 shows lab data during application of eight injection rates. The breakthrough

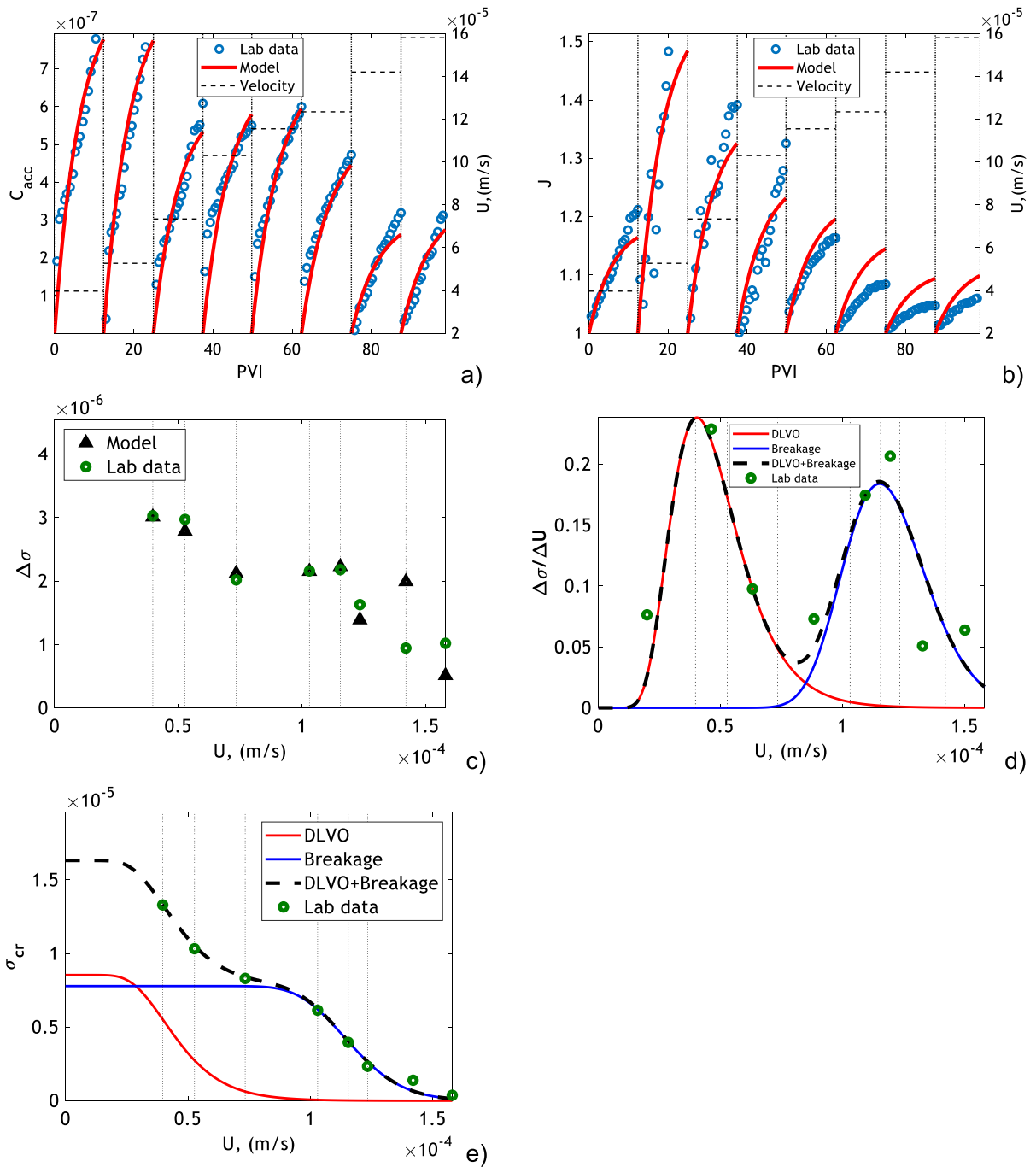


Fig. 8 Matching lab data on authigenic and detrital fines migration in coal cores: **a** accumulated breakthrough concentrations for 8 flow rates; **b** impedance; **c** detached particle concentration under each of 8 rates; **d** approximation of detached

density function by the total of two log-normal distributions; **e** maximum retention functions (MRFs) for detrital and authigenic fines, and the total MRF

Table 1 The tuning result of matching accumulated concentration and impedance

U (m/s)	3.97×10^{-5}	5.27×10^{-5}	7.34×10^{-5}	1.03×10^{-4}	1.16×10^{-4}	1.23×10^{-4}	1.42×10^{-4}	1.58×10^{-4}
α	4.7×10^{-3}	4.7×10^{-3}	4.7×10^{-3}	4.7×10^{-3}	4.7×10^{-3}	4.7×10^{-3}	4.7×10^{-3}	4.7×10^{-3}
β	0.71×10^5	1.94×10^5	1.94×10^5	1.28×10^5	0.92×10^5	0.65×10^5	0.65×10^5	0.78×10^5
λ (1/m)	647.87	639.15	625.5	606.49	598.64	593.73	582.32	572.69
$\Delta\sigma$	3.03×10^{-6}	2.97×10^{-6}	2.02×10^{-6}	2.16×10^{-6}	2.18×10^{-6}	1.62×10^{-6}	9.45×10^{-7}	1.02×10^{-6}
$R^2(C_{acc})$	0.92	0.95	0.93	0.78	0.94	0.91	0.92	0.92
$R^2(J)$	0.92	0.55	0.87	0.80	0.98	0.98	0.99	0.98

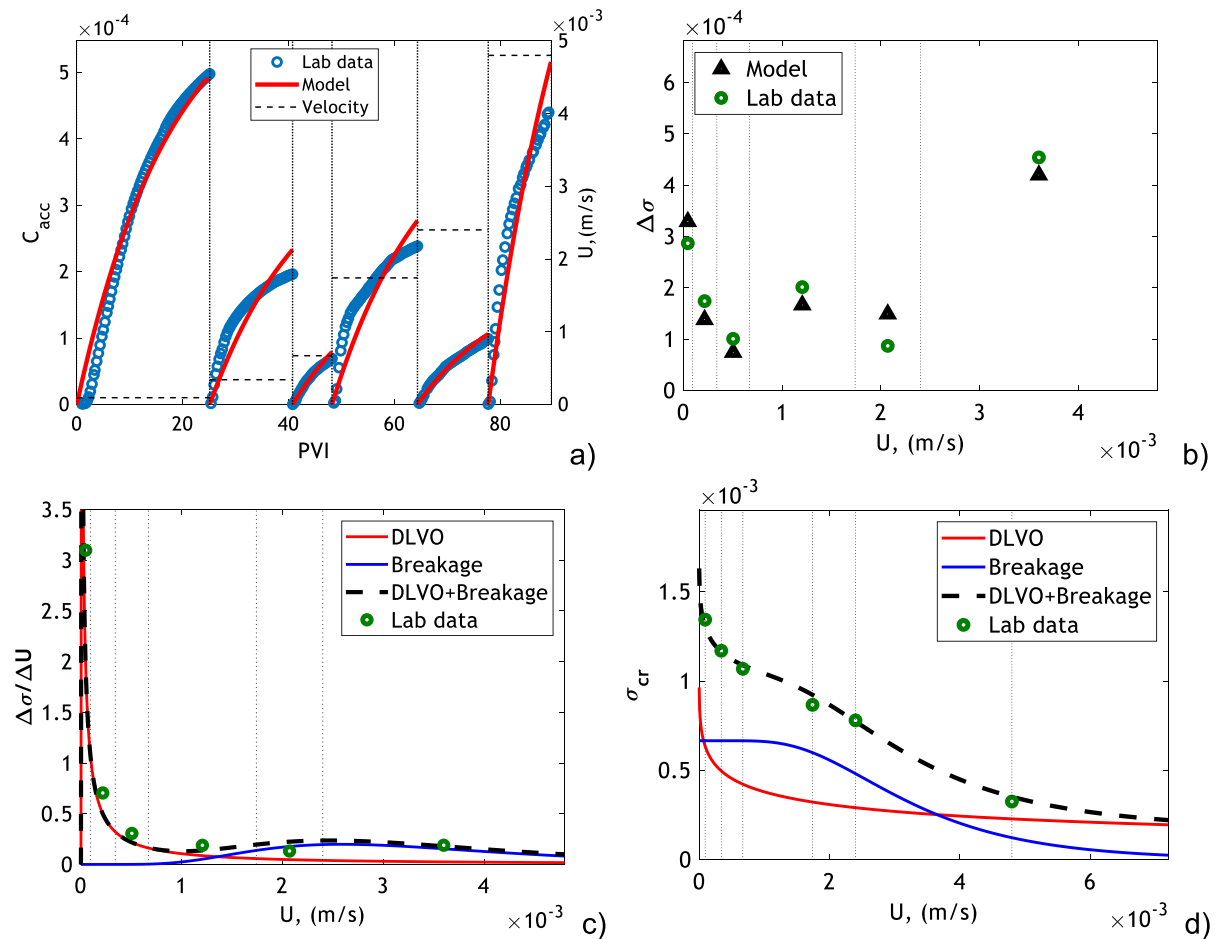


Fig. 9 Matching lab data on authigenic and detrital fines migration in sandstone cores: **a** accumulated breakthrough concentrations for 6 flow rates; **b** detached particle concentration under each of 6 rates; **c** approximation of detached density

function by the total of two log-normal distributions; **d** maximum retention functions (MRFs) for detrital and authigenic fines, and the total MRF

concentration and pressure drop across the core, have been measured during the overall test. Figure 8a shows breakthrough concentration data and their matching by the model. Figure 8b presents the history of impedance.

Figure 8a shows exponential growth of the accumulated breakthrough concentrations, which corresponds to exponential decrease of the momentum breakthrough concentrations $c_n(x=1,t)$. This behaviour is typical for deep bed filtration of low-concentration colloids with constant filtration coefficient (Chen et al. 2008; You et al. 2015).

The mathematical model (30–34) contains four dimensionless parameters—the drift delay factor, α , the formation damage factor, β , the filtration coefficient, λ , and the detached concentration during each stage, $\Delta\sigma(U_n)$ —which must be tuned for each flow rate U_n , $n=1, 2 \dots 8$. Table 1 presents the tuning results. Figure 8c shows the tuned and measured values of detached particle concentrations. The probabilistic density of velocity distribution of the detached fines are presented in Fig. 8d. The PDF is bimodal, which is attributed to fines detachment by breakage and against electrostatic forces, where the particles are authigenic and detrital, respectively. The PDF allows the approximation by the total of two log-normal distributions with high accuracy. Figure 8e shows two individual MRFs and their total, which is MRF for the overall colloid. Eight experimental points for the total detached concentrations match well with the accumulated MRF curve.

Tensile strength T_0 along with the bond radius r_b can be calculated from Eq. (15) and the histogram for detachment velocity (Fig. 8d). Assume the typical value of coefficient of variation of the bond radius as $C_v=0.03$ (Ting et al. 2022). Equation (15) can be used for mean detachment velocity, which is taken from the breakage-velocity histogram in Fig. 8d— $U_{mean}^b=1.21 \times 10^{-4}$ m/s. Minimum value of detachment velocity— $U_{min}^b=0.63 \times 10^{-4}$ m/s—corresponds to minimum value of bond radius, which can be estimated as $r_b(1-3C_v r_b)$. Applying Eq. (15) to mean and minimum breakage velocities allows calculating two unknowns $T_0=0.03$ MPa and $r_b=3.0 \times 10^{-7}$ m. Stability of calculations of tensile strength and bond radius from mean and minimum breakage velocities is determined by high difference in their values— U_{mean}^b is 1.92 times higher than U_{min}^b .

Torkzaban et al. (2015) conducted lab tests on consolidated (sandstone) core sample from the Yarragadee Formation (Perth Basin, Western Australia). The laboratory study was comprised of water injection with concentrations 47 mg/L of sodium chlorite and 9 mg/L of calcium chlorite into the sandstone core with permeability 2697 mD and porosity 0.32. Core length was 7 cm. Figure 9 shows lab data during application of six injection rates. Table 2 presents the results of tuning the model coefficients. The breakthrough concentration has been measured during the overall test. The data on pressure drop across the core are not available from the original paper.

Figure 9 shows lab data and their matching by the model (30–34) during application of six injection rates: breakthrough concentration data (Fig. 9a), detached concentrations at each rate (Fig. 9b), density distributions for detachment velocity for authigenic and detrital fines (Fig. 9c), and individual MRFs for authigenic and detrital fines along with overall MRF.

Like in the previous test, the detachment velocity distribution has a clear bimodal structure, which also supports the two-population hypothesis.

Table 2 presents the tuning results for dimensionless parameters— α , β , λ , and $\Delta\sigma(U_k)$ —which have been determined for each flow rate U_k , $k=1, 2 \dots 8$.

Applying Eq. (15) for mean and minimum detachment velocities, which are taken from the histogram in Fig. 9c— $U_{mean}^b=2.75 \times 10^{-3}$ m/s and $U_{min}^b=1.22 \times 10^{-3}$ m/s, respectively—we obtain $T_0=0.56$ MPa and $r_b=1.35 \times 10^{-7}$ m.

For both tests, the tuned parameters vary within common intervals, earlier presented in the literature (Chen et al. 2008; Bradford et al. 2013; You et al. 2015; Guo et al. 2016). The obtained tensile strength for kaolinite is also typical (Han et al. 2019; Yang et al. 2019). The detached concentrations $\Delta\sigma_{cr}(U)$ versus velocity for both kinds of particles increases at small rates from zero and declines at high velocities, which complies with typical form of the maximum retention curve (Bedrikovetsky et al. 2011, 2012). High values of the coefficient of determination show high match between the experimental and modelling data, which validates the model.

Close match by single-population model has been achieved for lab data of 16 corefloods with piecewise-constant increasing rates (Table 5). The tuned

Table 2 The tuning result of matching accumulated concentration

U (m/s)	9.26×10^{-5}	3.4×10^{-4}	6.7×10^{-4}	1.74×10^{-3}	2.4×10^{-3}	4.8×10^{-3}
α	4.1×10^{-2}	4.11×10^{-2}	4.11×10^{-2}	4.13×10^{-2}	4.15×10^{-2}	4.2×10^{-2}
β	0	0	0	0	0	0
λ (1/m)	19.52	19.5	19.46	19.36	19.3	19.3
$\Delta\sigma$	2.87×10^{-4}	1.74×10^{-4}	1.01×10^{-4}	2.02×10^{-4}	0.87×10^{-4}	4.54×10^{-4}
$R^2(C_{acc})$	0.97	0.78	0.96	0.77	0.97	0.90

Table 3 Flow velocities in faults in different basins

No	References	Basin	Velocity, m/s
1	Matthäi and Roberts (1996)	Gulf of Mexico Basin, USA	3.2×10^{-6} – 3.2×10^{-4}
2	Liu et al. (2018)	Anju Coal Mine, China	0.5×10^{-4} – 4×10^{-4}
3	Yu et al. (2020)	Dongtan Coal Mine, China	1×10^{-3} – 1.2×10^{-2}
4	Eichhubl and Boles (2000)	Monterey Formation, Coastal California, USA	0.01
5	Maloszewski et al. (1999)	Lange Bramke Basin, Germany	0.15

parameters have the same order of magnitude as those presented in Tables 1 and 2.

5 Breakage of authigenic clays in geological faults

Mobilization and migration of authigenic clays cause the permeability decrease in geological faults and faulted zones, which is important for sealing capacities of CO₂ and hydrogen storage, and for interpretation of various seismic events (Farrell et al. 2021). Let us discuss whether authigenic clay detachment by breakage due to viscous water flux under fault conditions is feasible.

Table 3 presents water velocities in faults in different basins as reported in papers the referred papers. Papers by Matthäi and Roberts (1996), Liu et al. (2018), and Yu et al. (2020) took the velocity values from the basin data to use in simulation, via paper by Eichhubl and Boles (2000) retrieved the velocity directly from tracer test, and paper by Maloszewski et al. (1999) inferred it by the size of entrained rock fragments. Maloszewski et al. (1999) present the probability distribution function (PDF) for velocity detachment by breakage and the velocities of water in faults as presented all 5 papers. The data for calculations are presented in Table 4 and taken from publications Ting et al. (2021) and Farrell et al. (2021). Ting et al. (2021) shows that particle radius, aspect ratio, bond radius and their variation coefficients, presented

Table 4 Particle parameters to calculate PDF for breakage velocity

Parameter	Mean value	Coefficient of variation (C _v)
Particle radius r_s (μm)	2	0.17
Aspect ratio α_s	0.65	0.17
Tensile strength T_0 (Mpa)	0.2	–
Bond radius r_b (μm)	0.16	0.02

in Table 4, are the most influential parameters on PDF.

Figure 10 shows that breakage of kaolinite in the case 1 almost does not occur; some authigenic fines are broken in the case 2. Significant part of authigenic fines is broken in the case 3. In the cases 4 and 5, all authigenic particles are detached by breakage.

6 Determining the fractions of detachable clays and authigenic fines in rocks

Tuning the model coefficients by matching the lab coreflood data by the analytical model for 1D deep bed filtration with constant filtration coefficient λ , given by Eqs. (34–38) allows calculating the fraction of detachable fines with respect to initial clay content in the rock (column 9 in Table 5), fraction of detached fines produced during corefloods (column 10), and fraction of authigenic fines in the

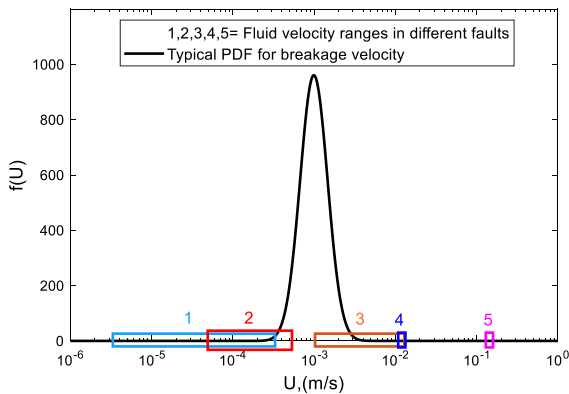


Fig. 10 Probability distribution function (PDF) for breakage velocity and flow velocities in the geological faults

overall detachable fines (11th column). Table 5 presents the results of 16 coreflood data matching. Tests 1–3 have been performed by Ochi and Vernoux (1998), test 4—by Torkzaban et al. (2015), tests 5 and 6—by Shang et al. (2008), tests 7, 8—by Huang et al. (2017), tests 9, 10—by Huang et al. (2018), test 11—by Guo et al. (2016), tests 12–14—by Huang et al. (2021), tests 15, 16—by Hashemi et al. (2022, 2023a).

The fraction of detachable fines in consolidated rocks and high-salinity water injection varies from 0.01 to 0.19% (Lines 1–3, 6–11, 15, and 16), which agrees with the previously published data (Russell et al. 2017). This percentage is so low due to small fraction of clay particles located at the rock surface, where they are accessible to water flux; vast majority of clays are located inside the rock skeleton and matrix. In grinded rocks and high-salinity water injection, the fraction increases up to 19–75% (Lines 12–14) due to high accessibility of grain surfaces to the water flux in porous space. In high porosity sandstone and packed sediment, the fraction increases to 18 and 90% under low-salinity and deionized water injection (Lines 4 and 5, respectively) due to disappearance of DLVO particle-rock attraction at low salinities.

The fraction of authigenic fines of the overall concentration of detached fines varies from 0.36 to 0.83. For those rocks, the ratio between the maximum rate at the coreflood and minimum breakage velocity exceeds one, indicating fines b) breakage (11th column in Table 5). Authigenic particles

haven't been observed in packed sediments and in artificial packed sediment cores (Lines 5, 6 and 9, 10, respectively). In other 12 cases, the minimum breakage velocity is below the maximum velocity applied in the corresponding test, so authigenic fines have been observed in the production.

The breakage velocity of authigenic fines is widely distributed—11th column of Table 5 shows that the ratio of maximum and minimum breakage velocities varies from 1.2 to 4.5, i.e., the calculation method for tensile strength T_0 and bond radius r_b using Eq. (15) is stable.

The analytical model for 1D fines migration with constant particle capture (filtration) coefficient λ , given by Eq. (35) for $c(x,t)$, allows calculating the ratio between the stabilised accumulated concentration of produced fines and the detached overall detached concentration (8th column in Table 5):

$$\frac{\phi_{c_{acc}}}{\sigma_0} = \frac{1 - \exp(-\lambda L)}{\lambda L}, \quad (18)$$

so the ratio depends on the dimensionless filtration coefficient λL only, where L is the system length. Plot of curve (18) and the points from 6th column are placed in Fig. 11a. The curve and the 16-test data show the clear tendency that the higher is the filtration coefficient the faster is the particle capture and the lower fraction of the mobilised fines is produced. The fraction varies from one for zero filtration coefficient, to zero where the filtration coefficient tends to infinity. Some point scattering and mismatch with the curve is explained by heterogeneous colloid, including varying particle properties and different forms and capture probabilities for detrital and authigenic fines.

The stabilised impedance is also calculated from the analytical model (35–38) for

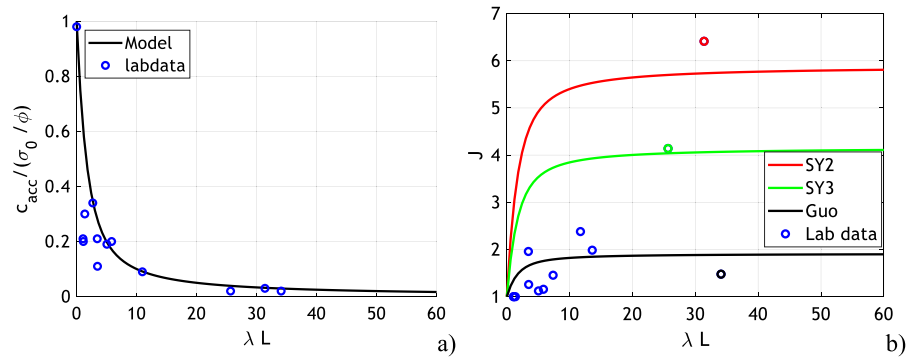
$$J(t \rightarrow \infty) = J_{st} = 1 + \beta \Delta \sigma \left[1 - \frac{1 - e^{-\lambda L}}{\lambda L} \right] \quad (19)$$

Besides the dimensionless filtration coefficient, the stabilised impedance (19) depends on formation damage coefficient β and the detached fines concentration $\Delta \sigma$, which explained the scattering of the points in Fig. 11b. The curve $J_{st}(\lambda L)$ increases from 1 at zero filtration coefficient to $1 + \beta \Delta \sigma$ where filtration coefficient tends to infinity. Figure 11b presents three

Table 5 The fraction of detachable kaolinite rocks, fraction of detached fines produced during corefloods, and fraction of authigenic fines in the produced particle concentration

No	Rock type	Salinity	Clay fraction, C_c	Porosity, ϕ	Produced fines, $\sum C_a$	Detach-able fines, σ_0	$\sum C_a \phi / \sigma_0$	$\sigma_0 / [C_c(1-\phi)] \times 100$	Authi-genic fraction, σ_0^b / σ_0	U_{max} / U_{min}^b
1	Berea core	0.5 M	0.08	0.2	–	1.08×10^{-4}	–	0.17	0.36	2.46
2		0.1 M	0.08	0.2	–	7.5×10^{-5}	–	0.12	0.5	3.78
3		0.01 M	0.08	0.2	–	1.02×10^{-4}	–	0.16	0.35	1.99
4	Sandstone core	8×10^{-4} M	0.013	0.32	1.55×10^{-3}	1.65×10^{-3}	0.3	18	0.41	3.98
5	Packed sedi-ment	DI	0.03	0.45	6.53×10^{-3}	1.5×10^{-2}	0.19	90	0	–
6		0.5 M	0.03	0.45	4.57×10^{-6}	9.9×10^{-6}	0.21	0.06	0	–
7	Anthri-cite coal core	0.27 M	4.64×10^{-2}	0.1	4.62×10^{-6}	1.63×10^{-5}	0.03	0.04	0.48	2.51
8		0.27 M	4.64×10^{-2}	0.1	4.58×10^{-6}	1.86×10^{-5}	0.02	0.04	0.5	1.19
9		0.27 M	4.64×10^{-2}	0.24	3.62×10^{-6}	4.04×10^{-6}	0.21	0.01	0	–
10		0.27 M	4.64×10^{-2}	0.24	5.92×10^{-6}	7.35×10^{-6}	0.19	0.02	0	–
11	Bitumi-nous coal core	0.01 M	6.8×10^{-2}	2.4×10^{-2}	6.2×10^{-7}	7.61×10^{-7}	0.02	1.1×10^{-3}	0.56	1.57
12	Grinded bitumi-nous coal	0.27 M	0.13	0.38	1.5×10^{-2}	6.1×10^{-2}	0.09	75	0.68	2.22
13		0.27 M	0.13	0.36	4.45×10^{-2}	1.63×10^{-2}	0.98	19	0.83	2.00
14		0.27 M	0.13	0.33	1.92×10^{-2}	1.88×10^{-2}	0.34	21	0.59	2.22
15	Castle gate core	0.6 M	6.6×10^{-2}	0.24	2.8×10^{-5}	5.9×10^{-5}	0.09	0.15	0.77	2.22
16		0.6 M	6.6×10^{-2}	0.24	8.04×10^{-5}	9.72×10^{-5}	0.17	0.22	0.51	4.45

Fig. 11 Effects of particle capture by the rock on fines migration: **a** fraction of produced fines in the detached concentration versus dimensionless filtration coefficient; **b** impedance (reciprocal to normalised average permeability) versus filtration coefficient



curves corresponds to tuning of three lab cases; the curves correspond to points with the same colour.

The above plots show how the number of produced fines and permeability decline vary with filtration coefficient—increase of filtration coefficient yields decrease of produced fines and growth of permeability damage. Several papers claim insignificant fines migration based on the data of low produced concentrations. Yet, low produced concentration could be due to high filtration coefficient, so fines migration must be indicated by the impedance increase along with the number of produced fines.

Mineral dissolution chemical reactions weaken the rocks, decreasing strength in Eq. (15) and resulting in additional fines liberation in situ the reservoir yielding the additional sweep enhancement. Those increase the fraction of authigenic fines. The dissolution reactions make CO_2 and hydrogen storages susceptible to fines breakage.

7 Effects of colloidal breakage detachment on reservoir and well behaviour

1D radial problem for fines detachment and flow toward well allows for exact solution under constant production rate (You et al. 2015, 2019). Detached fines straining results in permeability decline and increase of the pressure drop between the well and the reservoir. Treatment of 16 coreflood tests, presented in Table 5, yields calculation of filtration and formation damage coefficients along with maximum retention functions for detachment against electrostatic forces and by breakage, like it was performed in Sect. 4. Implementing these values into the solution for fines migration in radial flow permits the

estimation of wellbore impedance as well as the relative impacts of authigenic and detrital fines on well injectivity. For the parameter values of case 16 in Table 5 the critical retention function and impedance are presented in Fig. 12a and b respectively. The red curves in this plot correspond to the experimental conditions of the test by Hashemi et al. (2023a) (salinity, $\gamma=0.6$ M, viscosity, $\mu_f=1$ cp, and temperature $T=25$ °C). The critical retention function shows a clear distinction between the detachment of detrital particles at low velocity and detachment of authigenic particles for higher velocities. For this $\sigma_{cr}(U)$ curve, the corresponding impedance in Fig. 12b is close to one, indicating negligible formation damage. This is a result of the high velocities required for particle detachment.

The conditions of the experimental test are not indicative of those in most field injection scenarios. Due to explicit calculation of the critical retention function based on physical considerations, the effect of changing environmental conditions can be examined by changing relevant parameters. In this way the results of experiments can be extended beyond the conditions they were performed under. Here we consider three different scenarios covering a range of applications.

The three cases considered are low salinity (corresponding to freshwater recharge wells), high viscosity (corresponding to the injection of fracturing fluid), and high temperature (corresponding to geothermal or deep petroleum wells). Changing salinity to 0.01 M decreases the velocities required to detach detrital particles but has no effect on authigenic particles, as illustrated by the critical retention function in Fig. 12a. Increasing viscosity increases drag and lift, increasing detachment of all particles. Lastly

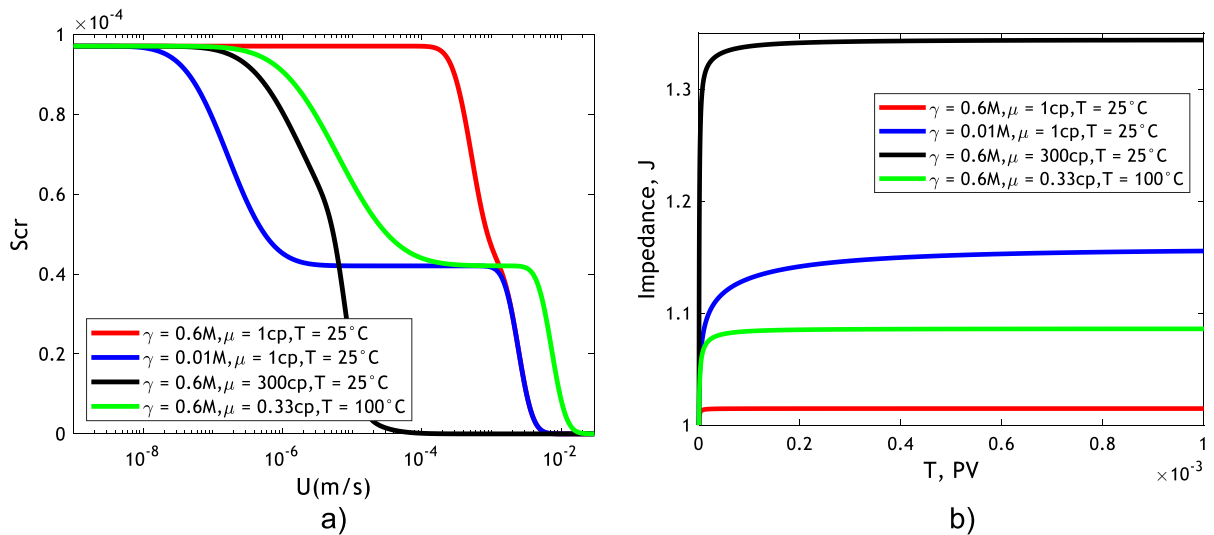


Fig. 12 Formation damage during injection of water under different conditions: **a** critical retention functions, **b** impedance

increasing temperature mostly affects detrital particles, as it decreases the electrostatic force, but it also results in a decrease in the viscosity, slightly affecting authigenic particles. All three cases result in larger values of impedance as shown in Fig. 12b. This demonstrates the importance of fines migration across a range of applications.

Changes of these system parameters clearly do not affect authigenic and detrital detachment uniformly. Thus, we consider the relative importance of each kind of detachment under the three reservoir conditions. Impedance curves showing the predicted impedance if particles detached only by DLVO (detrital) or breakage (authigenic) are shown in Fig. 13. At low salinity, breakage is negligible, and all formation damage occurs due to detrital particles which are weakly held to the rock's surface at low γ . For high viscosity, both detrital and authigenic particles contribute to formation damage, with more than half of the damage caused by breakage. Lastly, Fig. 13c shows that the formation damage at high temperatures results almost entirely from the weakening of electrostatic forces.

Geological site selection for CO_2 and hydrogen storage highly depends on well performance and storage capacity. Authigenic fines breakage along with detrital particle detachment can cause significant permeability reduction with detrimental well productivity and injectivity decline, but to storage capacity

increase. High velocity in highly permeable layers and patterns yields higher fines detachment and permeability reduction, resulting in homogenisation of injectivity and productivity profiles and, finally, in enhanced sweep (Bedrikovetsky 2013). In the case of CO_2 injection, sweep increase leads to enhancement of the pore volume where capillary, stratigraphic and chemical CO_2 capture occurs, increasing the storage capacity. In the case of cyclic hydrogen injection and production, sweep enhancement results in increase of water-free hydrogen production.

The competitive effects of well index decline and sweep enhancement with CO_2 and hydrogen storage are in odds with each other: the higher is the injection rate, the higher is the sweep and storage capacity, but the higher is the well index decrease. The optimal injection and production rates can be determined using the mathematical modelling that includes Eqs. (12–15).

8 Breakage of authigenic fines during well exploitation

In this section we investigate whether fines breakage can occur in the vicinity of production and injection wells for different reservoir conditions. Table 6 presents the data for heavy oil production (Ado 2021), polymer injection (Gao 2021), dewatering of coal bed

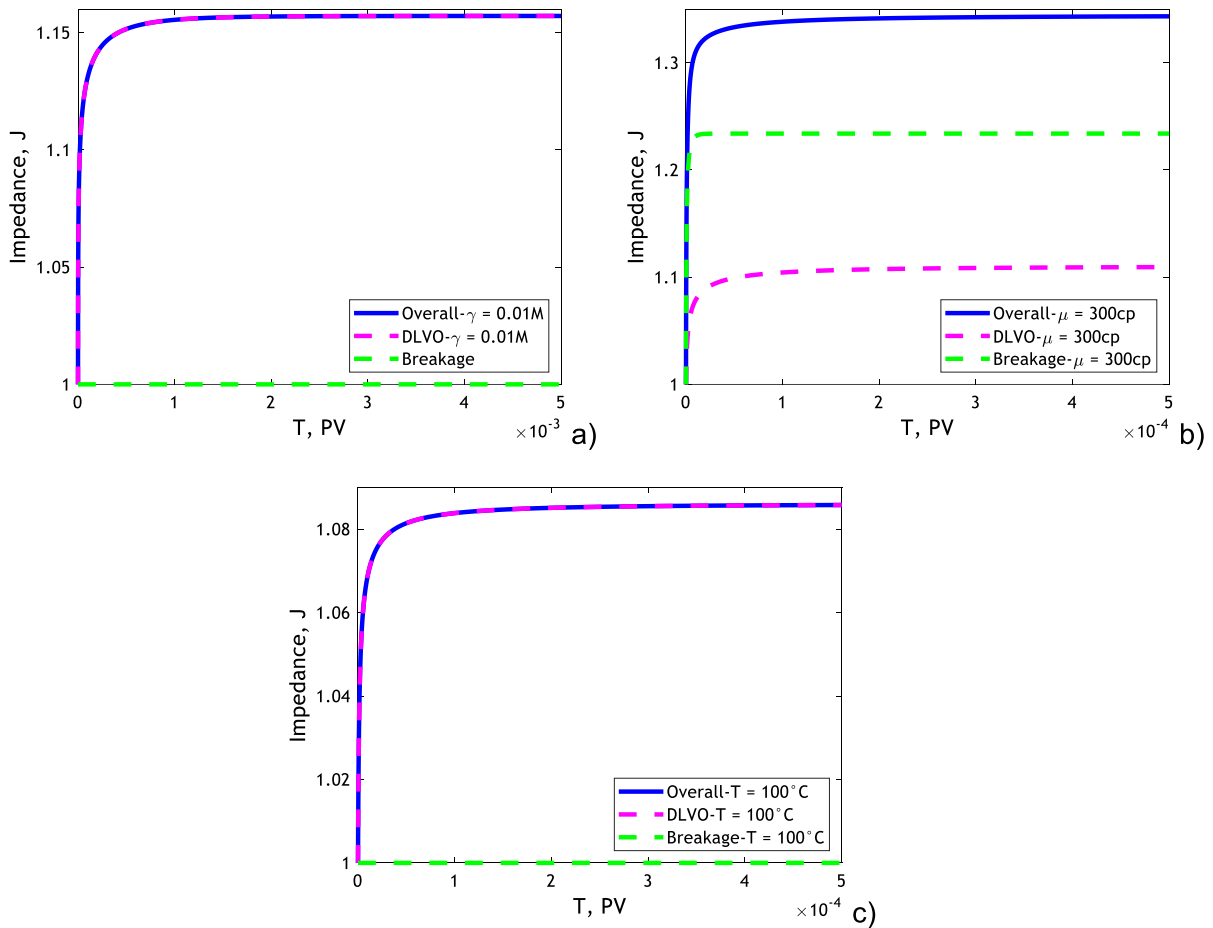


Fig. 13 Impact on injectivity of detachment via two mechanisms: DLVO (detrital particles) and breakage (authigenic particles) under different conditions, **a** low salinity water injection, **b** injection of high viscosity fluid, **c** injection under high temperatures

methane (CBM) reservoir (Shi et al. 2008), injection of supercritical CO_2 into carbonate reservoir (Spivak et al. 1989), hydraulic fracturing using water as a fracturing fluid (HFW) (Prasetyo et al. 2021), hydraulic fracturing using high-viscosity fracturing fluid (HF) (Prasetyo et al. 2021), natural gas production (NG) (Peischl et al. 2015), water production from geothermal reservoirs (GWP) (Ishido et al. 1992), water injection into aquifers (WI) (De Lino 2005), and water production from aquifers (WP) at low and high rates (Kulakov and Berdnikov 2020). The data for calculations are taken from those literature sources. For all cases, spherical particle shape ($\alpha_s = 1$) corresponds to kaolinite booklet; typical fine size is taken as $r_s = 2 \mu\text{m}$.

The breakage velocity is calculated using Eqs. (12–15) and is given in nineths column. The well rates are taken from the corresponding papers. Column nine shows the velocity on well walls for well radius $r_w = 0.1 \text{ m}$.

The velocity on the well wall exceeds minimum breakage velocity for heavy oil production, polymer injection, both cases of hydraulic fracturing, production of natural gas and geothermal water, water injection into aquifers and water production from artesian well with high rate, so fines breakage can occur under those conditions. The velocity on well wall is lower than minimum breakage velocity for dewatering in CBM, CO_2 injection, and water production with low rates.

Table 6 Occurrence of fines breakage in well vicinity

No	Well type	α_s	δ	ν	χ	μ_f (Pa.s)	T_0 (Mpa)	U_{min}^b (m/s)	U_w (m/s)
1	Heavy oil	1	0.05	0.25 [29]	6.54×10^{-4}	0.30	0.2	1.01×10^{-6}	5.67×10^{-6}
2	Polymer	1	0.05	0.24 [30]	6.57×10^{-4}	0.04	0.2	6.69×10^{-6}	8.8×10^{-5}
3	CBM	1	0.05	0.35 [22]	6.27×10^{-4}	1×10^{-3}	0.2	3.57×10^{-4}	1.14×10^{-5}
4	CO ₂	1	0.05	0.21 [31]	6.67×10^{-4}	1.49×10^{-4}	0.2	8.51×10^{-4}	4.74×10^{-5}
5	HFW	1	0.05	0.33 [24]	6.32×10^{-4}	1×10^{-3}	0.2	8.93×10^{-4}	1.38×10^{-2}
6	HF	1	0.05	0.33 [14]	6.32×10^{-4}	1	0.2	8.93×10^{-7}	1.38×10^{-2}
7	NG	1	0.05	0.23 [32]	6.6×10^{-4}	1.21×10^{-4}	0.2	2.72×10^{-4}	1.33×10^{-3}
8	GWP	1	0.05	0.25 [33]	6.54×10^{-4}	1.2×10^{-4}	0.2	1.49×10^{-4}	4.44×10^{-4}
9	WI	1	0.05	0.286[34]	6.44×10^{-4}	1×10^{-3}	0.2	1.96×10^{-4}	7.02×10^{-4}
10	WP _{min}	1	0.05	0.34 [35]	6.29×10^{-4}	1×10^{-3}	0.2	1.34×10^{-4}	3.68×10^{-5}
11	WP _{max}	1	0.05	0.34 [35]	6.29×10^{-4}	1×10^{-3}	0.2	1.34×10^{-4}	3.32×10^{-4}

Similar effects of well injectivity and productivity as well as in situ bond strength decline by chemical reactions occur during geothermal exploitation, where fines detachment occurs due to DLVO forces decrease at high temperature, and in fractured reservoirs that are highly susceptible to fines breakage due to high flow velocity (Atree-Williams et al. 2019; Wang et al. 2022c). During water and CO₂ injection in carbonate reservoirs, where rock dissolution yields massive release of various size particles, the effects of particle mobilisation by breakage is expected to be significantly more pronounced.

9 Discussions

The current version of the breakage-detachment model is limited to single-phase flows. Adding the capillary force exerting by menisci on the attached fines into torque balance (16) would cover the detachment by breakage during gas flow in shale rocks and CO₂ and hydrogen storage (Roshan et al. 2016; Siddiqui et al. 2019). The appropriate two-phase flow model accounts for moving interface (Shapiro 2015, 2018).

The primary limitation of the model is brittle behaviour of the particle–substrate bond during breakage; the study of ductile bonds would complicate the failure criteria (6) and phase diagrams. Accounting for non-elasticity of the rock and non-Newtonian fluid, the rheology yields in more complex expressions for stress maxima than (12–15); in this case the breakage regime will be velocity-dependent.

The model developed in this paper is limited to single-population colloidal transport, given by Eqs. (30–32) with further separation of MRF into those by authigenic and detrital fines, while Hashemi et al. (2023a) apply two-population balance model with two different filtration functions for authigenic and detrital populations. A more general approach would encompass multicomponent colloidal transport with non-linear fines straining (Bedrikovetsky et al. 2019).

The analytical model for well inflow performance under fines migration using the model constants obtained from 12 corefloods, where the authigenic fines mobilisation have been observed (Table 5), yields well index decrease up to 1.4 times. We expect significantly higher effects based on more representative corefloods. Besides, all 16 tests have been performed in sandstones. Significantly higher formation damage is expected during waterflooding or CO₂ injection in carbonates, where rock dissolution yields reduction of particle-rock bond radius with consequent bond breakage and massive fines release.

Numerous geomechanics studies determine the strength and other failure parameters of the rocks, while the bond-breakage criteria in Eq. (12–15) contain those for a single particle and substrate. Those measurements require significantly more sophisticated equipment (Su et al. 2022; Roshan et al. 2023). Currently, those parameters for mineral particles are unavailable. Derivation of the fine-breakage model in Sect. 2 may stimulate those experimental studies.

The breakage-detachment models (11–15) and (17, 33) correspond to particle and rock scales, respectively. The current work does not include a method for

calculating maximum retention function from torque balance, and vice versa—calculation of mechanical equilibrium coefficients of the attached particles from the MRF. A recent work by Hashemi et al. (2023b) presents a stochastic model for the mechanical equilibrium of detrital particles, where the equilibrium conditions are given by Eq. (16). Averaging yields the MRF for detrital fines. Performing similar theoretical development for authigenic fines accounting for mechanical equilibrium given by Eqs. (12–15) would result in an expression for maximum retention function for fines detachment by breakage.

10 Conclusions

The model derivations for particle detachment by breakage, integrating the Timoshenko's beam theory with CFD flow modelling and strength criteria, and applying the model to different geo-energy topics allow concluding as follows.

Maximum stresses are reached either at the beam base middle $Y=0$ or at its boundary. Breakage conditions, where either of tensile or shear stresses reaches the strength value, are determined by three dimensionless parameters: strength-drag number κ , aspect-Poisson number χ , and strength ratio η . The tensile-stress diagram in plane (χ, ν) determines which of tensile stresses is higher. The shear-stress diagram in plane (χ, η) determines 4 breakage regimes depending on aspect-Poisson number χ , Poisson's ratio ν , and strength ratios η .

The definition of breakage regime—by either tensile or shear stress—is independent of flow velocity. For an identified breakage regime, breakage velocity is determined by the strength-drag number $\kappa(\chi, \nu)$ alone. For a given particle shape, the critical breakage velocity is proportional to strength and particle size, and it is inversely proportional to viscosity.

The expression for critical breakage velocity allows determining the breakage maximum retention function MRF, which is a mathematical model for particle detachment by breakage of particle-rock surface bond. MRF closes the governing system for colloidal transport with breakage detachment.

The lab-based analytical model for fines breakage shows that under strong subterranean water fluxes, the authigenic fines mobilisation by breakage can occur in geological faults, resulting in permeability

decline and affecting sealing capacities during CO₂ and hydrogen injection for storage.

Matching of 16 coreflood tests exhibits high agreement between the laboratory and modelling data. Besides, the model coefficient values as obtained by tuning, belong to their common intervals of variation. This validates the developed model for migration of authigenic and detrital fines in rocks.

The matching allows determining the detachable fines fraction in the overall clay content, and the authigenic fines fraction in the detachable fines. The detachable fines fraction in consolidated rocks and high-salinity water injection varies from 0.01 to 0.19%. It increases up to 19–90% in grinded rocks or by deionised water injection. The authigenic fines fraction of the detachable clay particles varies in the interval 0.4–0.8.

In 12 corefloods from 16, where authigenic fines have been found, the breakthrough curves during corefloods exhibit two-population behaviour, which is attributed to commingled production of the authigenic and detrital particles. Besides, size distributions of produced fines are bimodal.

Analytical 1D model for axi symmetric flow allows recalculating coreflood tests with migration of authigenic and detrital fines into the well productivity curve, permitting estimating the formation damage due to fines migration.

Calculations of minimum breakage velocities/well rates using Eq. (15) for typical values of the breakage-model parameters show high feasibility of rock fines breakage during heavy oil production, polymer injection, both cases of hydraulic fracturing, production of natural gas and geothermal water, water injection into aquifers and water production from artesian well with high rate.

Funding Open Access funding enabled and organized by CAUL and its Member Institutions No funding was received for conducting this study.

Data availability The data used to support the findings of this study are available from the corresponding author upon request.

Declarations

Ethics approval Not applicable.

Consent to publish All authors agree to publish this manuscript in journal of Geomechanics and Geophysics for Geo-Energy and Geo-Resources.

Appendix 1: CFD calculations for drag and its torque

The formulae for drag and torque factors in Eq. (1) for spheroidal and thin cylindrical particles are available from Ting et al. (2021). In this work, those factors for long thin cylinders, which model illite clay particles, are calculated for $\alpha_s > 1$:

$$f_d = (0.9014\alpha_s^2 + 1.599\alpha_s + 2.265)(\alpha_s + 1.752)^{-1} \tag{20}$$

$$f_M = (0.0002161\alpha_s^3 + 1.34\alpha_s^2 + 44.18\alpha_s + 21.27)(\alpha_s^2 + 31.34\alpha_s + 10.38)^{-1} \tag{21}$$

Appendix 2: Stresses in elastic beam by Timoshenko’s model

Stress distributions in cylindric elastic beam (Timoshenko and Goodier 1970) are

$$\sigma_z = \frac{F_d b f_M x}{I} \tag{22}$$

$$\tau_{xz} = \frac{(3 + 2\nu) F_d}{8(1 + \nu) I} \left(r_b^2 - x^2 - \frac{(1 - 2\nu)}{(3 + 2\nu)} y^2 \right) \tag{23}$$

$$\tau_{yz} = -\frac{(1 + 2\nu) F_d x y}{4(1 + \nu) I} \tag{24}$$

$$\sigma_x = \sigma_y = \tau_{xy} = 0 \tag{25}$$

The stress tensor, as per solution (12–15) is:

$$\begin{bmatrix} 0 & 0 & \tau_{xz} \\ 0 & 0 & \tau_{yz} \\ \tau_{xz} & \tau_{yz} & \sigma_z \end{bmatrix} \tag{26}$$

The principal stresses are eigen values of the stress tensor (26):

$$\sigma_1 = \frac{\sigma_z + \sqrt{\sigma_z^2 + 4(\tau_{xz}^2 + \tau_{yz}^2)}}{2}, \quad \sigma_2 = 0, \tag{27}$$

$$\sigma_3 = \frac{\sigma_z - \sqrt{\sigma_z^2 + 4(\tau_{xz}^2 + \tau_{yz}^2)}}{2}$$

where, $\sigma_1, \sigma_2, \sigma_3$ are principal stresses in order of decreasing of their values, and

$$\sigma_1 > \sigma_2 = 0 > \sigma_3. \tag{28}$$

The equation for largest Mohr circle for the case of $\sigma_2 = 0$ is

$$\left[\sigma - \left(\frac{\sigma_1 + \sigma_3}{2} \right) \right]^2 + \tau^2 = \left[\frac{(\sigma_1 - \sigma_3)}{2} \right]^2 \tag{29}$$

where σ and τ are tensile and shear stresses acting on unitary planes with different orientations.

Appendix 3: Population balance model for colloidal-suspension transport in porous media

We discuss deep bed filtration of the total particle population for detrital and authigenic fines. The state variables are the volumetric concentrations of suspended and strained particle, c and σ_s , respectively, and the pore pressure p . Mass balance and capture rate equations and Darcy’s law for the colloidal flux are:

$$\frac{\partial}{\partial t} (\phi c + \sigma_s) + \frac{\partial}{\partial x} (c \alpha U_n) = 0 \tag{30}$$

$$\frac{\partial \sigma_s}{\partial t} = \lambda c \alpha U_n, \quad n = 0, 1, 2 \dots \tag{31}$$

$$U_n = -\frac{k_0}{(1 + \beta \sigma_s) \mu_f} \frac{\partial p}{\partial x} \tag{32}$$

where ϕ is the porosity, λ is the constant filtration coefficient, α is the drift-delay factor, U_n is the flow velocity at n -th injection, k_0 is the initial undamaged permeability, p is the pressure, and β is the formation damage coefficient. Index n is attributed to injection

velocity, and $U_0=0$. The filtration coefficient for the low-concentration fines population is constant.

Initial suspended concentration is equal to concentrations of mobilised fines after velocity increase. It is posed at each moment $\phi L/\alpha U_{n-1}$ of the velocity switch from U_{n-1} to U_n

$$t = t_n : c_{n0} = \frac{\sigma_{cr}(U_{n-1}) - \sigma_{cr}(U_n)}{\phi} = \frac{\Delta\sigma_{cr}(U_n)}{\phi} \tag{33}$$

Here the overall MRF is a total of two individuals MRFs by Eq. (17).

Inlet boundary condition corresponds to injection of particle-free water

$$x = 0, \quad t_n < t < t_{n+1} : c_n = 0 \tag{34}$$

$$\sigma_{s,n}(x, t) = \begin{cases} \sigma_{s,n-1}(x, t_n) + \Delta\sigma_{cr}(U_n) \left(1 - \exp\left(-\frac{\lambda\alpha U_n}{\phi}(t - t_n)\right)\right), & x > \frac{\alpha U_n}{\phi}(t - t_n) \\ \sigma_{s,n-1}(x, t_n) + \Delta\sigma_{cr}(U_n)(1 - \exp(-\lambda x)), & x < \frac{\alpha U_n}{\phi}(t - t_n) \end{cases} \tag{36}$$

The exact solution of the problem (30–34) can be found in handbooks Polyanin and Manzhirov (2006), or Polyanin and Zaitsev (2012). Breakthrough concentration is obtained by the method of characteristics:

$$c_n(x, t) = \begin{cases} \frac{\Delta\sigma_{cr}(U_n)}{\phi} \exp\left(-\frac{\lambda\alpha U_n}{\phi}(t - t_n)\right), & x > \frac{\alpha U_n}{\phi}(t - t_n) \\ 0, & x < \frac{\alpha U_n}{\phi}(t - t_n) \end{cases} \tag{35}$$

Breakthrough concentration becomes zero at the moment of the concentration front arrival at the moment $\phi L/\alpha U_n$. At this moment, all concentrations and pressure drop stabilise. Yet, even where the switch times $t_{n+1}-t_n$ are lower than the arrival times, we neglect suspension concentration which was formed before the switch.

Strained concentration is obtained integration of Eq. (31) in t accounting for expression (35):

The dimensionless pressure drop (impedance) J is defined as:

$$J(t) = \frac{\Delta p(t) U(0)}{\Delta p(0) U(t)} \tag{37}$$

The expression for impedance is derived from Eq. (32) by integrating pressure gradient in x from $x=0$ to core length $x=L$:

$$J_n(t) = \begin{cases} J_{n-1}(t_n) + \beta \Delta\sigma_{cr}(U_n) I_n(t), & t - t_n < \frac{L\phi}{\alpha U_n} \\ J_{n-1}(t_n) + \beta \Delta\sigma_{cr}(U_n) \left(\left(1 + \frac{1}{\lambda L} \exp(-\lambda L) - \frac{1}{\lambda L}\right) \right), & t - t_n > \frac{L\phi}{\alpha U_n} \end{cases} \tag{38}$$

$$I_n(t) = \frac{\alpha U_n}{\phi L}(t - t_n) + \frac{1}{\lambda L} \exp\left(-\lambda \frac{\alpha U_n}{\phi}(t - t_n)\right) - \frac{1}{\lambda L} + \left(1 - \frac{\alpha U_n}{\phi L}(t - t_n)\right) \left[1 - \exp\left(-\frac{\lambda\alpha U_n}{\phi}(t - t_n)\right)\right]$$

Open Access This article is licensed under a Creative Commons Attribution 4.0 International License, which permits use, sharing, adaptation, distribution and reproduction in any medium or format, as long as you give appropriate credit to the original author(s) and the source, provide a link to the Creative Commons licence, and indicate if changes were made. The images or other third party material in this article are included in the article's Creative Commons licence, unless indicated otherwise in a credit line to the material. If material is not included in the article's Creative Commons licence and your intended use is not permitted by statutory regulation or exceeds the permitted use, you will need to obtain permission directly from the copyright holder. To view a copy of this licence, visit <http://creativecommons.org/licenses/by/4.0/>.

References

- Abousleiman YN, Hull KL, Han Y, Al-Muntasheri G, Hosemann P, Parker S, Howard CB (2016) The granular and polymer composite nature of kerogen-rich shale. *Acta Geotech* 11(3):573–594
- Ado MR (2021) Improving heavy oil production rates in THAI process using wells configured in a staggered line drive (SLD) instead of in a direct line drive (DLD) configuration: detailed simulation investigations. *J Petrol Explor Prod Technol* 11(11):4117–4130
- Altree-Williams A, Brugger J, Pring A, Bedrikovetsky P (2019) Coupled reactive flow and dissolution with changing reactive surface and porosity. *Chem Eng Sci* 206:289–304
- Alzate-Espinosa GA, Araujo-Guerrero EF, Torres-Hernandez CA, Benítez-Peláez CA, Herrera-Schlesinger MC, Higuera-Carvajal E, Naranjo-Agudelo A (2023) Impact assessment of strain-dependent permeability on reservoir productivity in CSS. *Geomech Geophys Geo-Energy Geo-Resour* 9(1):67
- Appelo CAJ, Postma D (2004) *Geochemistry, groundwater and pollution*. CRC Press, Boca Raton
- Bedrikovetsky P (2013) *Mathematical theory of oil and gas recovery: with applications to ex-USSR oil and gas fields, vol 4*. Springer, Berlin
- Bedrikovetsky P, Siqueira FD, Furtado CA, Souza ALS (2011) Modified particle detachment model for colloidal transport in porous media. *Transp Porous Media* 86(2):353–383
- Bedrikovetsky P, Zeinijahromi A, Siqueira FD, Furtado CA, de Souza ALS (2012) Particle detachment under velocity alternation during suspension transport in porous media. *Transp Porous Media* 91(1):173–197
- Bedrikovetsky P, Osipov Y, Kuzmina L, Malgaresi G (2019) Exact upscaling for transport of size-distributed colloids. *Water Resour Res* 55(2):1011–1039
- Bradford SA, Torkzaban S, Shapiro A (2013) A theoretical analysis of colloid attachment and straining in chemically heterogeneous porous media. *Langmuir* 29(23):6944–6952
- Cao Z, Xie Q, Xu X, Sun W, Fumagalli A, Fu X (2023) Mass-loss effects on the non-Darcy seepage characteristics of broken rock mass with different clay contents. *Geomech Geophys Geo-Energy Geo-Resour* 9(1):32
- Chen C, Packman AI, Gaillard JF (2008) Pore-scale analysis of permeability reduction resulting from colloid deposition. *Geophys Res Lett* 35(7):66
- Chen X, Peng D, Morrissey JP, Ooi JY (2022) A comparative assessment and unification of bond models in DEM simulations. *Granular Matter* 24(1):1–20
- De Lino RAU (2005) Case history of breaking a paradigm: improvement of an immiscible gas-injection project in Buracica field by water injection at the gas/oil contact. In: *SPE Latin American and Caribbean petroleum engineering conference*. OnePetro
- Drummond J, Schmadel N, Kelleher C, Packman A, Ward A (2019) Improving predictions of fine particle immobilization in streams. *Geophys Res Lett* 46(23):13853–13861
- Duan Y, Feng XT, Li X, Ranjith PG, Yang B, Gu L, Li Y (2022) Investigation of the effect of initial structure and loading condition on the deformation, strength, and failure characteristics of continental shale. *Geomechan Geophys Geo-Energy Geo-Resour* 8(6):207
- Eichhubl P, Boles JR (2000) Rates of fluid flow in fault systems; evidence for episodic rapid fluid flow in the Miocene Monterey Formation, coastal California. *Am J Sci* 300(7):571–600
- Farrell NJC, Debenham N, Wilson L, Wilson MJ, Healy D, King RC, Holford SP, Taylor CW (2021) The effect of authigenic clays on fault zone permeability. *J Geophys Res Solid Earth* 126(10):e2021JB022615
- Feng R, Zhang Y, Rezagholilou A, Roshan H, Sarmadivaleh M (2020) Brittleness index: from conventional to hydraulic fracturing energy model. *Rock Mech Rock Eng* 53(2):739–753
- Fjaer E, Holt RM, Horsrud P, Raaen AM (2008) *Petroleum related rock mechanics*. Elsevier, Amsterdam
- Fox A, Packman AI, Boano F, Phillips CB, Arnon S (2018) Interactions between suspended kaolinite deposition and hyporheic exchange flux under losing and gaining flow conditions. *Geophys Res Lett* 45(9):4077–4085
- Gao CH (2011) Scientific research and field applications of polymer flooding in heavy oil recovery. *J Petrol Explor Prod Technol* 1(2):65–70
- Guo Z, Hussain F, Cinar Y (2016) Physical and analytical modelling of permeability damage in bituminous coal caused by fines migration during water production. *J Nat Gas Sci En* 35:331–346
- Hadi YA, Hussain F, Othman F (2019) Low salinity water flooding in carbonate reservoirs—dissolution effect. In *IOP conference series: materials science and engineering*, vol 579, No. 1. IOP Publishing,
- Han Z, Yang H, He M (2019) A molecular dynamics study on the structural and mechanical properties of hydrated kaolinite system under tension. *Mater Res Express* 6(8):0850c3
- Hashemi A, Borazjani S, Nguyen C, Loi G, Badalyan A, Dang-Le B, Bedrikovetsky P (2022) Fines migration and production in CSG reservoirs: laboratory & modelling study. In: *SPE Asia Pacific oil & gas conference and exhibition*. OnePetro
- Hashemi A, Borazjani S, Nguyen C, Loi G, Khazali N, Badalyan A, Yang Y, Tian ZF, Ting HZ, Dang-Le B, Russell T (2023a) Geo-mechanical aspects for breakage

- detachment of rock fines by Darcy's flow. arXiv preprint [arXiv:2301.01422](https://arxiv.org/abs/2301.01422)
- Hashemi A, Nguyen C, Loi G, Khazali N, Yang Y, Dang-Le B, Russell T, Bedrikovetsky P (2023b) Colloidal detachment in porous media: Stochastic model and upscaling. *Chem Eng J* 474:145436
- Hou X, Qi S, Huang X, Guo S, Zou Y, Ma L, Zhang L (2022) Hydrate morphology and mechanical behavior of hydrate-bearing sediments: a critical review. *Geomech Geophys Geo-Energy Geo-Resour* 8(5):161
- Hu K, Liu D, Tian P, Wu Y, Deng Z, Wu Y et al (2021) Measurements of the diversity of shape and mixing state for ambient black carbon particles. *Geophys Res Lett* 48(17):e2021GL094522
- Huang F, Kang Y, You Z, You L, Xu C (2017) Critical conditions for massive fines detachment induced by single-phase flow in coalbed methane reservoirs: modeling and experiments. *Energy Fuels* 31(7):6782–6793
- Huang F, Kang Y, You L, Li X, You Z (2018) Massive fines detachment induced by moving gas-water interfaces during early stage two-phase flow in coalbed methane reservoirs. *Fuel* 15(222):193–206
- Huang F, Dong C, You Z, Shang X (2021) Detachment of coal fines deposited in proppant packs induced by single-phase water flow: theoretical and experimental analyses. *Int J Coal Geol* 239:103728
- Iglauer S, Pentland CH, Busch A (2015) CO₂ wettability of seal and reservoir rocks and the implications for carbon sequestration. *Water Resour Res* 51(1):729–774
- Iglauer S, Ali M, Keshavarz A (2021) Hydrogen wettability of sandstone reservoirs: implications for hydrogen geo-storage. *Geophys Res Lett* 48(3):e2020GL090814
- Iglauer S, Akhondzadeh H, Abid H, Paluszny A, Keshavarz A, Ali M et al (2022) Hydrogen flooding of a coal core: effect on coal swelling. *Geophys Res Lett* 49(6):e2021GL096873
- Ishido T, Kikuchi T, Miyazaki Y, Nakao S, Hatakeyama K (1992) Analysis of pressure transient data from the Sumikawa geothermal field (No. SGP-TR-141-26). Geological Survey of Japan, Tsukuba, Ibaraki, JP; Mitsubishi Materials Corporation, Kazuno, Akita, JP
- Israelachvili JN (2015) Intermolecular and surface forces, 3rd ed, pp 1–676
- Jaeger JC, Cook NG, Zimmerman R (2009) Fundamentals of rock mechanics. Wiley, New York
- Johnson WP, Pazmino E (2023) Colloid (nano- and micro-particle) transport and surface interaction in groundwater. The Groundwater project, Guelph, Ontario, Canada, 2023
- Kulakov VV, Berdnikov NV (2020) Hydrogeochemical processes in the Tunguska reservoir during in situ treatment of drinking water supplies. *Appl Geochem* 120:104683
- Kumari WGP, Beaumont DM, Ranjith PG, Perera MSA, Avanthi Isaka BL, Khandelwal M (2019) An experimental study on tensile characteristics of granite rocks exposed to different high-temperature treatments. *Geomech Geophys Geo-Energy Geo-Resour* 5:47–64
- Lehmann P, Leshchinsky B, Gupta S, Mirus BB, Bickel S, Lu N, Or D (2021) Clays are not created equal: How clay mineral type affects soil parameterization. *Geophys Res Lett* 48(20):e2021GL095311
- Li N, Xie H, Hu J, Li C (2022) A critical review of the experimental and theoretical research on cyclic hydraulic fracturing for geothermal reservoir stimulation. *Geomech Geophys Geo-Energy Geo-Resour* 8:1–19
- Liao X, Shi Y, Liu CP, Wang G (2021) Sensitivity of permeability changes to different earthquakes in a fault zone: Possible evidence of dependence on the frequency of seismic waves. *Geophys Res Lett* 48(9):e2021GL092553
- Liu W, Zhao J, Nie R, Liu Y, Du Y (2018) A coupled thermal-hydraulic-mechanical nonlinear model for fault water inrush. *Processes* 6(8):120
- Liu J, Yuan X, Zhang J, Xi W, Feng J, Wu H (2019) Sharp reductions in high-productivity well due to formation damage: case study in Tarim Basin, China. In: Proceedings of the international field exploration and development conference 2017. Springer, Singapore, pp 843–857
- Lu Y, Moernaut J, Bookman R, Waldmann N, Wetzler N, Agnon A et al (2021) A new approach to constrain the seismic origin for prehistoric turbidites as applied to the Dead Sea Basin. *Geophys Res Lett* 48(3):e2020GL090947
- Maloszewski P, Herrmann A, Zuber A (1999) Interpretation of tracer tests performed in fractured rock of the Lange Bramke basin, Germany. *Hydrogeol J* 7:209–218
- Matthäi SK, Roberts SG (1996) The influence of fault permeability on single-phase fluid flow near fault-sand intersections: results from steady-state high-resolution models of pressure-driven fluid flow. *AAPG Bull* 80(11):1763–1779
- Mishra S, Ojha K (2016) A novel chemical composition to consolidate the loose sand formation in the oil field. In: International petroleum technology conference. OnePetro
- Obermayr M, Dressler K, Vrettos C, Eberhard P (2013) A bonded-particle model for cemented sand. *Comput Geotech* 49:299–313
- Ochi J, Vernoux JF (1998) Permeability decrease in sandstone reservoirs by fluid injection: hydrodynamic and chemical effects. *J Hydrol* 208(3–4):237–248
- Othman F, Yu M, Kamali F, Hussain F (2018) Fines migration during supercritical CO₂ injection in sandstone. *J Nat Gas Sci Eng* 56:344–357
- Othman F, Naufaliansyah MA, Hussain F (2019) Effect of water salinity on permeability alteration during CO₂ sequestration. *Adv Water Res* 127:237–251
- Peischl J, Ryerson TB, Aikin KC, De Gouw JA, Gilman JB, Holloway JS, Lerner BM, Nadkarni R, Neuman JA, Nowak JB, Trainer M (2015) Quantifying atmospheric methane emissions from the Haynesville, Fayetteville, and northeastern Marcellus shale gas production regions. *J Geophys Res Atmos* 120(5):2119–2139
- Polyanin AD (2002) Linear partial differential equations for engineers and scientists. Chapman and Hall/CRC, London
- Polyanin AD, Manzhirov AV (2006) Handbook of mathematics for engineers and scientists. Chapman and Hall/CRC, London
- Polyanin AD, Zaitsev VF (2012) Handbook of nonlinear partial differential equations. Chapman & Hall/CRC Press, Boca Raton
- Prasetyo MH, Anggraini H, Tjahjono H, Pramadana AB, Akbari A, Madyanova M, Mekarsari R, Akbarizal A, Setiawan P (2021) Success story of optimizing hydraulic fracturing design at Alpha low-permeability reservoir. In:

- SPE/IATMI Asia Pacific oil & gas conference and exhibition. OnePetro
- Ren J, He H, Senetakis K (2021) A Micromechanical-based investigation on the frictional behaviour of artificially bonded analogue sedimentary rock with calcium carbonate. *Pure Appl Geophys* 178(11):4461–4486
- Roshan H, Al-Yaseri AZ, Sarmadivaleh M, Iglauer S (2016) On wettability of shale rocks. *J Colloid Interface Sci* 475:104–111
- Roshan H, Li D, Canbulat I, Regenauer-Lieb K (2023) Borehole deformation based in situ stress estimation using televiewer data. *J Rock Mech Geotech Eng* 6:66
- Russell T, Pham D, Neishaboor MT, Badalyan A, Behr A, Genolet L, Kowollik P, Zeinijahromi A, Bedrikovetsky P (2017) Effects of kaolinite in rocks on fines migration. *J Nat Gas Sci Eng* 45:243–255
- Shang J, Flury M, Chen G, Zhuang J (2008) Impact of flow rate, water content, and capillary forces on in situ colloid mobilization during infiltration in unsaturated sediments. *Water Resour Res* 44(6):66
- Shapiro AA (2015) Two-phase immiscible flows in porous media: the Mesoscopic Maxwell–Stefan approach. *Transp Porous Media* 107:335–363
- Shapiro AA (2018) A three-dimensional model of two-phase flows in a porous medium accounting for motion of the liquid–liquid interface. *Transp Porous Media* 122(3):713–744
- Shi JQ, Durucan S, Fujioka M (2008) A reservoir simulation study of CO₂ injection and N₂ flooding at the Ishikari coalfield CO₂ storage pilot project, Japan. *Int J Greenhouse Gas Control* 2(1):47–57
- Siddiqui MAQ, Chen X, Iglauer S, Roshan H (2019) A multiscale study on shale wettability: spontaneous imbibition versus contact angle. *Water Resour Res* 55(6):5012–5032
- Spivak A, Karaoguz D, Issever K, Nolen JS (1989) Simulation of immiscible CO₂ injection in a fractured carbonate reservoir, Bati Raman Field, Turkey. In: SPE California regional meeting. OnePetro
- Su L, Lv A, Aghighi MA, Roshan H (2022) A theoretical and experimental investigation of gas adsorption-dependent bulk modulus of fractured coal. *Int J Coal Geol* 257:104013
- Sun X, Xiang Y (2021) Aquifer permeability decreases before local earthquakes inferred from water level response to period loading. *Geophys Res Lett* 48(15):e2021GL093856
- Tang Y, Lv C, Wang R, Cui M (2016) Mineral dissolution and mobilization during CO₂ injection into the water-flooded layer of the Pucheng Oilfield, China. *J Nat Gas Sci Eng* 33:1364–1373
- Teitelbaum Y, Shimony T, Saavedra Cifuentes E, Dallmann J, Phillips CB, Packman AI et al (2022) A novel framework for simulating particle deposition with moving bedforms. *Geophys Res Lett* 49(4):e2021GL097223
- Timoshenko SP, Goodier JN (1970) *Theory of elasticity*. McGraw, New York, pp 341–342
- Ting HZ, Bedrikovetsky P, Tian ZF, Carageorgos T (2021) Impact of shape on particle detachment in linear shear flows. *Chem Eng Sci* 241:116658
- Ting HZ, Yang Y, Tian ZF, Carageorgos T, Bedrikovetsky P (2022) Image interpretation for kaolinite detachment from solid substrate: type curves, stochastic model. *Colloids Surf A* 650:129451
- Torkzaban S, Bradford SA, Vanderzalm JL, Patterson BM, Harris B, Prommer H (2015) Colloid release and clogging in porous media: Effects of solution ionic strength and flow velocity. *J Contam Hydrol* 181:161–171
- Tu J, Yeoh GH, Liu C (2018) *Computational fluid dynamics: a practical approach*. Butterworth-Heinemann, London
- Turner LG, Steel KM (2016) A study into the effect of clean demineralisation by hydrochloric acid on the permeability of coal. *J Nat Gas Sci Eng* 36:931–942
- Wagner TJ, James TD, Murray T, Vella D (2016) On the role of buoyant flexure in glacier calving. *Geophys Res Lett* 43(1):232–240A
- Wang J, Huang Y, Zhou F, Song Z, Liang X (2020) Study on reservoir damage during acidizing for high-temperature and ultra-deep tight sandstone. *J Petrol Sci Eng* 191:107231
- Wang C, Xu X, Zhang Y, Arif M, Wang Q, Iglauer S (2022a) Experimental and numerical investigation on the dynamic damage behavior of gas-bearing coal. *Geomech Geophys Geo-Energy Geo-Resour* 8(2):49
- Wang T, Liu Y, Cai M, Zhao W, Ranjith PG, Liu M (2022b) Optimization of rock failure criteria under different fault mechanisms and borehole trajectories. *Geomech Geophys Geo-Energy Geo-Resour* 8(4):127
- Wang Y, Yin H, Othman F, Zeinijahromi A, Hussain F (2022c) Analytical model for fines migration due to mineral dissolution during CO₂ injection. *J Nat Gas Sci Eng* 100:104472
- Wang Y, Almutairi ALZ, Bedrikovetsky P, Timms WA, Privat KL, Bhattacharyya SK, Le-Hussain F (2022d) In-situ fines migration and grains redistribution induced by mineral reactions—Implications for clogging during water injection in carbonate aquifers. *J Hydrol* 614:128533
- Wilson MD, Pittman ED (1977) Authigenic clays in sandstones: recognition and influence on reservoir properties and paleoenvironmental analysis. *J Sediment Res* 47(1):3–31
- Wurgaft E, Wang ZA, Churchill JH, Dellapenna T, Song S, Du J et al (2021) Particle triggered reactions as an important mechanism of alkalinity and inorganic carbon removal in river plumes. *Geophys Res Lett* 48(11):e2021GL093178
- Xu X, Liu J, Jin X, Zhang Y, Arif M, Wang C, Iglauer S (2022) Dynamic mechanical response characteristics of coal upon exposure to KCl brine. *Geomech Geophys Geo-Energy Geo-Resour* 8(6):174
- Xue Y, Liu J, Ranjith PG, Gao F, Zhang Z, Wang S (2022) Experimental investigation of mechanical properties, impact tendency, and brittleness characteristics of coal mass under different gas adsorption pressures. *Geomech Geophys Geo-Energy Geo-Resour* 8(5):131
- Yang H, Han ZF, Hu J, He MC (2019) Defect and temperature effects on the mechanical properties of kaolinite: a molecular dynamics study. *Clay Miner* 54(2):153–159
- You Z, Badalyan A, Hand M (2015) Particle mobilization in porous media: temperature effects on competing electrostatic and drag forces. *Geophys Res Lett* 42(8):2852–2860
- You Z, Badalyan A, Yang Y, Hand M (2019) Fines migration in geothermal reservoirs: laboratory and mathematical modelling. *Geothermics* 77:344–367

- Yu H, Zhu S, Xie H, Hou J (2020) Numerical simulation of water inrush in fault zone considering seepage paths. *Nat Hazards* 104:1763–1779
- Yuan B, Moghanloo RG (2018) Nanofluid pre-coating: an effective method to reduce fines migration in radial systems saturated with two mobile immiscible fluids. *SPE J* 23(03):998–1018
- Yuan B, Moghanloo RG (2019) Analytical modeling nanoparticles-fines reactive transport in porous media saturated with mobile immiscible fluids. *AIChE J* 65(10):e16702
- Yuan H, Shapiro AA (2011) Induced migration of fines during waterflooding in communicating layer-cake reservoirs. *J Petrol Sci Eng* 78(3–4):618–626
- Zhai X, Atefi-Monfared K (2021) Production versus injection induced poroelasticity in porous media incorporating fines migration. *J Petrol Sci Eng* 205:108953
- Zhao Y, Liu S, Zhao GF, Elsworth D, Jiang Y, Han J (2014) Failure mechanisms in coal: dependence on strain rate and microstructure. *J Geophys Res Solid Earth* 119(9):6924–6935

Publisher's Note Springer Nature remains neutral with regard to jurisdictional claims in published maps and institutional affiliations.